



The interplay between ecological networks drives host-plasmid community dynamics


Ying-Jie Wang^{1*}, Kaitlin A. Schaal², Johannes Nauta^{3,}, Armun Liaghat⁴, Manlio De Domenico³, James P. J. Hall², Shai Pilosof^{1*}

1 Department of Life Sciences, Ben-Gurion University of the Negev, Beer-Sheva 84105, Israel

2 Department of Evolution, Ecology and Behaviour, Institute of Infection, Veterinary and Ecological Sciences, University of Liverpool, Liverpool L69 7ZB, UK

3 Department of Physics and Astronomy “Galileo Galilei”, University of Padova, Padova 35131, Italy

4 Department of Ecology and Evolution, University of Chicago, Chicago, IL 60637, USA

 These authors contributed equally to this work.

* lanexran@gmail.com, pilos@bgu.ac.il

Abstract

Plasmids drive evolution by transferring traits across microbial hosts. Transmission depends on both host–plasmid (infection) and plasmid–plasmid (compatibility) interactions, yet how the structure of these networks shapes transmission remains poorly understood. We hypothesized that these two ecological networks interact in non-additive ways to influence community outcomes. To test this, we developed a stochastic agent-based model that embeds both network structures and simulates coupled host–plasmid dynamics. We systematically varied the structure of each network, both individually and in combination, to isolate the effect of structure on host-plasmid dynamics. A modular (interactions organized into clusters) and hub (interactions concentrated on the highly connected) plasmid-plasmid compatibility network promoted transient host coexistence, while a modular host-plasmid infection network promoted plasmid diversity and stable host coexistence. Importantly, structured networks interacted non-additively, and their impact was most apparent when plasmid carriage imposed a moderate fitness cost on hosts. For example, combining a modular infection network with a hub compatibility network reversed the expected plasmid prevalence patterns, demonstrating that the structure of one network can counteract the effects of the other. We further re-parameterized our model to recapitulate empirical host-plasmid community dynamics, showing that infection network structure can strongly shape plasmid prevalence even in the presence of substantial biological heterogeneity. Our results highlight the necessity of jointly considering host–plasmid infection and plasmid–plasmid compatibility networks to understand host–plasmid community dynamics and their eco-evolutionary potential. More broadly, this work provides an initial mechanistic framework for generating testable hypotheses and underscores that systems involving multiple hosts and infectious agents require explicit consideration of how different ecological networks interact to shape community dynamics.

Author summary

Plasmids—genetic elements that can move between bacteria—help bacteria adapt and evolve by horizontally transferring traits such as metabolism or antibiotic resistance. Plasmid spread in microbiomes is shaped by interactions with bacterial hosts and other plasmids. However, how the combined structure of host–plasmid and plasmid–plasmid interactions influences microbial community dynamics remains unclear. We explored this fundamental question using a computational model and an experiment, to understand how two ecological networks interact: one network describing which plasmids infect which bacteria, and another describing which plasmids coexist with other plasmids inside bacteria. Our results demonstrate that understanding the dynamics of bacteria, plasmids, and other mobile genetic elements requires considering the interplay between multiple types of ecological networks. Our work provides a generalizable framework for understanding how diverse ecological interactions jointly shape community dynamics, directly addressing fundamental questions at the intersection of community ecology, network theory, and infectious disease dynamics.

Introduction

Plasmids play a vital role in the eco-evolutionary dynamics of host (bacteria) communities. As extrachromosomal mobile genetic elements (MGEs), plasmids can spread among host organisms, accelerating adaptation by transferring genes that confer advantageous traits such as antibiotic resistance [1, 2, 3]. Plasmids can also impose fitness costs on their hosts, which emerge from conflicts between chromosomal- and plasmid-encoded genes [4, 5]. However, these cost-benefit interactions between plasmids and their hosts are shaped by other microbiome interactions, such as plasmid co-infection and host competition, which together influence plasmid dynamics and the coexistence of their constituent hosts [6, 7, 8, 9, 10, 11, 12]. The impact of this interplay is often overlooked in studies of host-plasmid community dynamics.

Plasmids can interact with multiple hosts as they transfer across populations, creating patterns of host infection shaped by variation in within- and between-population conjugation rates, compatibility with host genetic backgrounds, and host anti-plasmid defense systems [13, 14, 15]. Plasmids can also compete with one another for hosts, using mechanisms such as (in)compatibility groups, toxin-antitoxin systems, and plasmid-encoded defense systems to exclude one another [16, 17, 18, 19, 20, 21, 22]. While some studies acknowledge the importance of multiple interaction types, they focus on simplified systems, such as multihost-uniplasmid [7] or unihost-bioplasmid systems [8]. However, in nature, hosts and plasmids form complex structures of interactions [23]. The few studies which consider multihost-multiplasmid systems omit or understate plasmid co-infection [24, 25, 26]. As a result, little is known about how the interplay of multiple interaction structures, specifically between host-plasmid interactions and plasmid co-infection, shapes community dynamics and stability. This gap hinders our ability to predict the assembly and evolutionary trajectories of these communities, particularly their potential in genetic innovation and adaptation. Nevertheless, addressing it is challenging because it requires connecting multiple interaction types in complex communities to dynamics—which is hard to do experimentally.

The interplay between different interaction types can be studied using ecological networks, which encode interactions (links) between multiple hosts and plasmids (nodes). Ecological networks are valuable tools for studying how network structure (i.e., the pattern in which interactions are distributed across species) affects community dynamics and species coexistence [27, 28]. Considering multiple ecological networks

allows us to study how distinct, interconnected networks affect community dynamics [12, 29, 30, 31]. However, there is a paucity in studies that explicitly link dynamics to the interplay between networks, leading to a gap in our understanding of structure-dynamics in complex ecological communities.

Our goals were to (1) test how variation in the structures of two fundamental interaction networks: the host–plasmid infection network and the plasmid–plasmid compatibility network—jointly shape host-plasmid dynamics, and (2) determine whether the joint effects of infection and compatibility networks can be inferred from either network in isolation. While other interaction types exist (e.g., host-host interactions such as competition [7, 32] and horizontal gene transfer (HGT) [24, 33]), we focus on infection (a host-plasmid interaction) and plasmid compatibility (a plasmid-plasmid-interaction, Fig 1a) because these interactions are significantly understudied in a network context despite being fundamental to host-plasmid communities.

Theory and empirical observations suggest that infection and compatibility networks regulate distinct but interconnected processes: infection structure governs which hosts plasmids can colonize, whereas compatibility structure dictates whether plasmids can coexist within hosts. Co-infection can, in turn, modify host growth, plasmid persistence, and opportunities for horizontal transfer [8, 9, 17]. Infection structure shapes the sequence and frequency with which plasmids encounter one another within hosts, while compatibility structure feeds back on infection success by altering plasmid persistence, competitive outcomes, and host-level costs. Consequently, the effect of a given structure in one network depends on the structure of the other, such that identical infection networks can give rise to different community-level dynamics under different compatibility architectures, and vice versa. This coupling provides a natural mechanism for non-additive effects, whereby combined outcomes cannot be inferred from either network in isolation. We therefore hypothesize that these networks jointly constrain the set of host subpopulations that plasmids can occupy, but do so in non-independent ways.

To test our hypothesis, we developed a stochastic, agent-based model that incorporates the structure of both networks and simulates the dynamics of host and plasmid populations (Fig 1). We systematically varied the structure of each of these networks, either individually or simultaneously, to isolate their independent and combined effects on community dynamics. Our model omits accessory genes that provide plasmids with advantages (e.g., antibiotic resistance), so that network structures can be compared within a homogeneous abiotic environment. While the model is broadly applicable to a wide range of hosts and infectious agents, we focus on bacteria and plasmids throughout.

Results

Network definitions

We first define the two networks used in our study. The host–plasmid infection network (**I**) is a bipartite network whose nodes consist of hosts and plasmids, and whose links indicate that a given plasmid can infect a given host. The plasmid–plasmid compatibility network (**P**) is a unipartite network whose nodes are plasmids, and whose links indicate that two plasmids are able to co-reside within the same host. To understand the relationship between network structure and dynamics in detail and from core principles, we intentionally used small networks (Fig 1a). While this choice was primarily conceptual, focusing on tractability and interpretability, it also aligned with practical considerations, as simulating larger networks becomes computationally intensive (see model limitations in materials and methods). Multiple biological

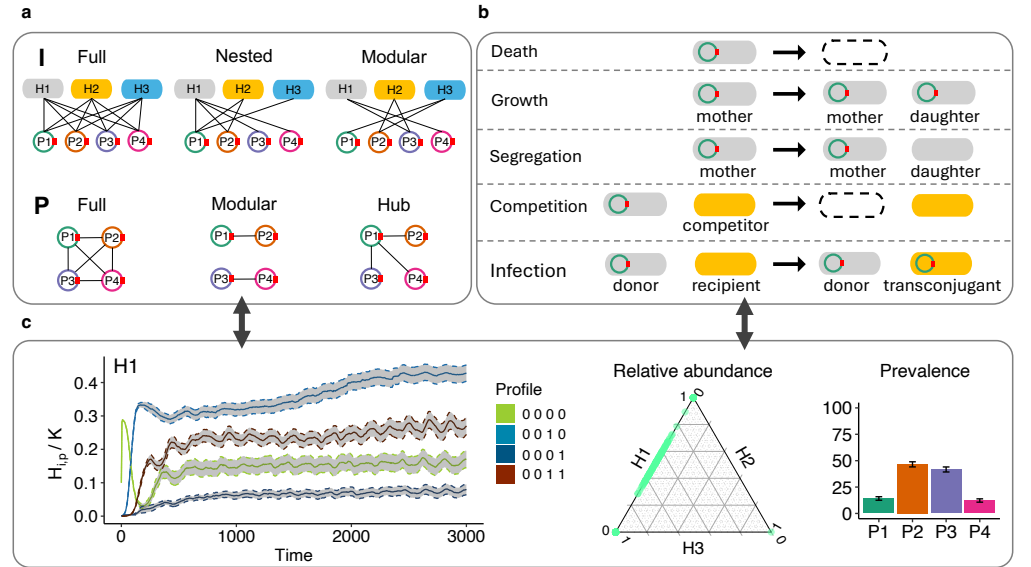


Fig 1. Model overview and experimental design. (a) The structures of the bacterial host-plasmid infection network **I** (which plasmid infects which hosts; top row) and plasmid-plasmid compatibility network **P** (which plasmids are compatible with each other and can therefore co-reside in a host individual; bottom row). H1, H2, H3 are the three hosts and P1, P2, P3, P4 are the four plasmids. The ‘full’ structures serve as controls. We used a factorial experimental design of the nine structure combinations. (b) Illustration of the five main events in the model (see Methods for detailed model explanations). Dashed ovals indicate deaths of individual cells. (c) An example of results of infection dynamics for the case of a modular **I** and full **P**, including subpopulation dynamics (left), final relative abundance of host populations of all replicates (middle), and the mean and SE of final plasmid prevalence across replicates at the end ($t = 20000$ hours) of the simulation (right).

processes can mediate plasmid infection, such as failure of transfer, long-term fitness costs, replication constraints, or incompatibility [23]. Below, we introduce the mechanisms behind some relevant structures. Note that we chose to focus on ‘non-infection’ as the relevant phenotype of interest, as this is what the infection network encodes, whilst remaining agnostic about the biological processes involved. We focused on the effects of the end structures (i.e., effective non-infection and incompatibility), because this is what the infection and compatibility networks encode.

Network structures

Infection network structures Previous studies of host-MGE infection networks have generally focused on phages, while the properties of multihost-multiplasmid infection networks remain poorly studied owing to technical difficulties in connecting plasmids with hosts (see [26, 34] for examples)[23]. Nevertheless, given that plasmids are also infectious MGEs, a similar theory can be used to represent the structure of host-plasmid interactions.

Host-phage networks often exhibit modular and nested structures [12, 35, 36] (e.g., Fig 1a, top row). A modular network is partitioned into clusters (modules) of microbes and MGEs that interact densely with each other but sparsely with those outside the module. Nestedness reflects instead patterns of specialization where specialist microbes are infected by subsets of MGEs that in turn also infect the more generalist microbes

[35]. These two structures are ultimately signatures of host-MGE coevolution and emerge from the co-evolutionary arms-race typical to infectious systems [12, 37, 38]. For example, bacteria-virus networks evolve nestedness under directional arms race dynamics, but not under fluctuating selection [39].

Modular infection networks can arise from a phylogenetic HGT barrier, where HGT occurs more often between closely related species [40, 41]. Theory shows that modularity can also emerge from the evolution of niches for phage growth, whereby bacteria are resources that a group of phages is able to infect because it has overcome bacterial defenses [12]. In plasmids, factors that affect HGT and immunity also exist and include plasmid mobility genes, replication genes, and CRISPR defense systems [23, 42, 43, 44]). This observation that modules reflect infection niches is supported by a study showing that antibiotic resistance (ABR) genes carried on plasmids would generate a more generalized infection pattern [34].

Nestedness indicates a hierarchy of infection patterns, which itself can reflect resistance hierarchy among hosts and infection ability among MGEs [36]. A nested structure can result from a sequence of adaptations whereby new bacterial mutations confer bacterial resistance to recently evolved phages while maintaining resistance to past phages. This is consistent with arms race coevolutionary dynamics, where hosts and phages evolve to increase their range of resistance [37, 38, 39]. A nested infection network can also arise from a trade-off between infecting many hosts and adapting to each host [45].

A rare multihost-multiplasmid study that has provided a census of plasmid-bacteria interactions in an infection network context [26] found that when putative ABR plasmids are excluded from the network, the network was more modular and less nested, because putative plasmids carrying ABR genes are advantageous and therefore, more widespread, connecting different parts of the network. In our study, we do not consider beneficial plasmid traits, which provides further support for choosing both modular and nested structures.

Given that modularity and nestedness are the dominant structures in host-MGE networks, and the empirical and theoretical evidence detailed above, we defined three structures for **I**: (1) ‘Full’, wherein all hosts can host all plasmids. This structure served as a reference (control). (2) ‘Nested’, wherein specialist plasmids interact with a subset of hosts with which more generalist plasmids interact [35, 36, 38, 39]. (3) ‘Modular’, wherein plasmid-host interactions form three distinct modules: two peripheral modules of hosts that are infected by distinct subsets of plasmids, and a bridge module where hosts can host a subset of plasmids from each of the peripheral modules (Fig 1a, top row). Host H2 and plasmids P2 and P3 in the bridge module are termed the bridge host and bridge plasmids.

Plasmids compatibility network structures Unlike infection networks, MGE co-infection networks are poorly studied. Although there are studies of plasmid co-infection [17, 46], no study has explicitly considered co-infection networks or analyzed their structures. We therefore suggest two plausible structures based on well-described molecular mechanisms. An important feature of plasmids is the immunity (e.g., CRISPR IV) and compatibility mechanisms they carry, which have a strong impact on the ability of plasmids to co-reside in a host cell due to shared replication or partitioning mechanisms [16, 18, 20, 21, 22, 47]. These molecular mechanisms can generate a modular structure via immunity or incompatibility group-mediated plasmid-plasmid interactions that impede a stable coexistence within the same host, as was also theoretically shown in phage-bacteria systems [12].

Another important feature influencing plasmid compatibility is the presence of genes that reduce conflict or promote functional complementarity. For instance, plasmids that

carry alternative replication or segregation systems that minimize interference with co-resident plasmids, or genes that encode functions complementing those of co-resident plasmids, are more likely to coexist with a broad range of plasmid types [8]. Such a feature can give rise to a ‘hub’ structure, in which the hub plasmids are rare among plasmids but disproportionately prevalent (i.e., widespread in the communities), as they can co-reside with many others. Novel incompatibility groups would encounter little direct conflict and thus be able to coexist broadly. This scenario is plausible because even small molecular changes can generate coexistence between otherwise identical plasmids. For example, a single-base pair mutation in the replication machinery was shown to produce a plasmid variant compatible with its own ancestor, effectively creating a new compatibility type [48].

Given the potential relevance of modular and hub structures in plasmid-plasmid networks, and the theoretical mechanisms detailed above, we defined three structures for \mathbf{P} : (1) ‘Full’, wherein all plasmids are compatible, serving as a reference (control). (2) ‘Modular’, wherein plasmids in the module are compatible with each other. (3) ‘Hub’, wherein a sole hub plasmid is the only one compatible with others, while non-hub plasmids have few interactions and can co-reside with only a limited set of plasmids.

The model links host-plasmid dynamics with network structures

To understand how network structures affect host-plasmid dynamics, we developed an agent-based model that incorporates five demographic and stochastic events: growth, death, plasmid loss by segregation, competition between hosts, and plasmid transmission by conjugation (Fig 1b). We employed a 3×3 factorial experimental design of the \mathbf{I} and \mathbf{P} structures. In each experiment we tracked the quantity $H_{i,p}$, which is the abundance of a microbial host population i that can be infected with a combination of plasmids, forming subpopulations with a plasmid profile p (Fig 1c). We included three hosts (H1-3) and four plasmids (P1-4). We used a binary notation system to describe the plasmid profile of each host subpopulation. For example, the total population abundance $H_i = \sum_p H_{i,p}$ of a host i might be split into two subpopulations 0000 and 0011. The first subpopulation is plasmid-free and the second is infected with plasmids P3 and P4.

To focus on the effects of network structure, we assumed that all plasmids and host populations have identical traits (e.g., growth and death rates, conjugation rates). That is, host and plasmid types exist in the same trait niche, differing only in their network niche (node position in the interaction networks). We modeled host competition for a shared limiting resource by applying a community-wide carrying capacity [49]. This formulation preserves the interdependence between plasmid costs and competitive pressure, which necessarily unfold across hosts drawing on the same resource pool. Assigning each host a separate carrying capacity would artificially decouple these biological feedbacks.

We assume that plasmids are costly, and do not consider the possible effects of beneficial accessory genes (e.g., antibiotic resistance). This allows us to isolate the network effects on plasmid persistence and community dynamics from the effects of positive selection for plasmid-encoded traits. Understanding plasmid maintenance in the absence of such selection is a necessary first step for assessing how network structure shapes community outcomes. The insights we obtain extend broadly to infectious agents that typically do not confer benefits to their hosts. Moreover, we applied a sufficiently high conjugation rate for infection, and a multiplicative cost for plasmid co-infection (representing a slight positive epistasis). Also, we assumed the host dynamics to be faster than infection dynamics, such that host dynamics go to equilibrium before infection dynamics do. Doing so allows us to focus very specifically on the consequences of the network structure.

For each experiment, we calculated: (1) relative host abundance: the relative abundance of each host population out of the total community abundance; (2) plasmid prevalence: the fraction of host individuals across all populations which are infected with the plasmid; (3) host population composition: the proportions of subpopulations, each defined by a plasmid profile, within the host population; (4) host coexistence probability: the fraction of simulations in which hosts coexisted at any given time point. We distinguish between transient coexistence, in which hosts coexist for a certain period of time (thus, a delayed extinction indicates a longer transient coexistence), and stable coexistence, in which by the end of the simulation two or three hosts have reached non-zero equilibrium densities.

Structured plasmid compatibility networks promote transient host coexistence

To understand the impact of the plasmid compatibility network \mathbf{P} on community dynamics, we compared community dynamics under various structures of \mathbf{P} while retaining a full infection network \mathbf{I} (Fig 2a). Under full \mathbf{I} and full \mathbf{P} (a control treatment), only one host population survived (Fig 2b(i); Fig S1). As expected, the identity of the host varied stochastically across replicate simulations, and the overall probability of a specific host surviving was about 1/3, because none of the hosts has an intrinsic advantage. Throughout the simulation, the probability of host transient coexistence rapidly decreased to zero (Fig 2b(i)). The host transient coexistence pattern was driven by neutral demographic stochasticity that eventually caused extinction, as well as by the high proportion of subpopulations infected by all four plasmids that induced higher costs and sped up extinction (Fig 2d(i); Fig S2). These heavily infected subpopulations acted as the main plasmid donors, continually re-infecting available hosts. At the final time point, all subpopulations (i.e., all possible plasmid profiles) of the surviving host were still present, and population composition was the same regardless of which specific host survived (Fig 2d(i)). The four plasmids reached the same prevalence, infecting slightly more than half of the individuals of the sole surviving host (Fig 2c(i)). This plasmid prevalence pattern was driven by all host individuals infected by one or multiple plasmids.

Introducing structure to plasmid compatibility drastically affected host transient coexistence patterns. When \mathbf{P} had a modular or hub structure, a random host population survived while the other two went extinct by the end of the simulation due to demographic stochasticity, but the process took up to 3 times longer (Fig 2b), reflecting an increased potential of transient coexistence. The average prevalence of the plasmids was similar to each other under each \mathbf{P} structure, except for P1 infecting 100% of its hosts as the hub plasmid (Fig 2c(ii-iii)). To explain the prolonged host coexistence and the plasmid prevalence patterns we compared the final population compositions to those resulting from the full \mathbf{P} experiment (Fig 2d). Although positive epistasis was implemented via multiplicative costs under co-infection (see eq. (2) in materials and methods), infections with four plasmids were still highly costly, accelerating host extinction. When \mathbf{P} is structured, no host subpopulation can be infected with all four plasmids. Instead, the surviving host population in each replicate simulation was comprised solely of subpopulations infected by two plasmids (either the two plasmids that shared a module, or the hub plasmid and one other; Fig 2d(ii-iii)).

Structure in the plasmid compatibility network \mathbf{P} could therefore alter host dynamics in nature through plasmid cost and patterns of conjugation. Moreover, while all of the communities ultimately collapsed to a single host population over the course of the simulations owing to the strict competition between hosts, \mathbf{P} structures qualitatively altered plasmid fates and prolonged the period of host coexistence. In a

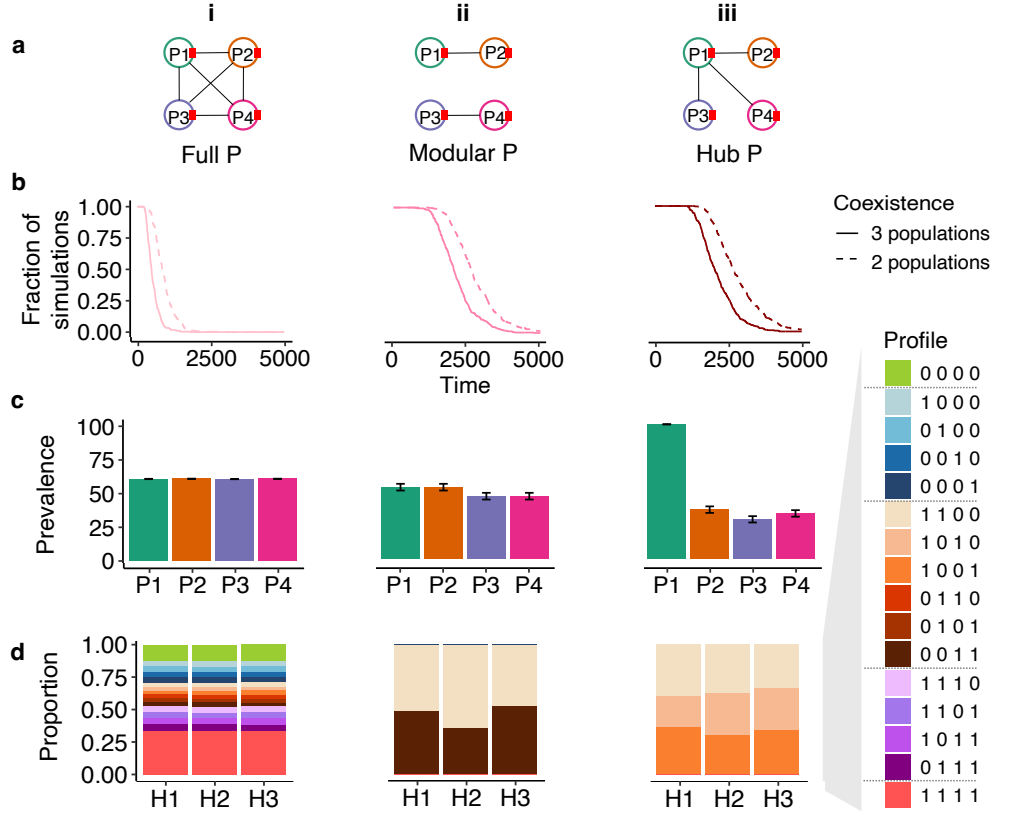


Fig 2. The effect of structure in the plasmid compatibility network P under a full infection network I . Columns i, ii, and iii represent different P structures. **(a)** Illustration of the different structures. **(b)** The dynamics of coexistence probability (fraction of simulations) of host populations. **(c)** Mean and SE of final plasmid prevalence across all replicates. **(d)** Final host population composition, averaged across replicates in which that host population survived (only populations surviving in > 5 replicates were considered). Profiles represent the host subpopulations (e.g., the profile 1000 represents a subpopulation hosting only P1).

natural community, these dynamic outcomes would provide greater opportunities for host and plasmid evolution.

A modular infection network promotes stable host coexistence and plasmid diversity

Next, we investigated the impact of infection network I (Fig 3a) on community dynamics. While under full I , each of the three host populations had an equal chance to out-compete the others, under nested I (hierarchical infections) the specialist host H3 consistently excluded the other two hosts (Fig 3b (i-ii)). As H3 could only be infected by the generalist plasmid P1, the other plasmids were lost from the community (Fig 3c(ii)). This outcome resulted from the lower net fitness cost to H3 of being susceptible to only one plasmid (Fig 3d(ii); Fig S3). Notably, this is under the model's assumption that all plasmids have the same cost to their hosts; more hosts and plasmids might survive if the generalist plasmid P1 has a much higher cost to H3 than other hosts. A nested infection network is therefore unlikely to be maintained without

influence from host-specific plasmid cost or external factors (see Discussion).

269

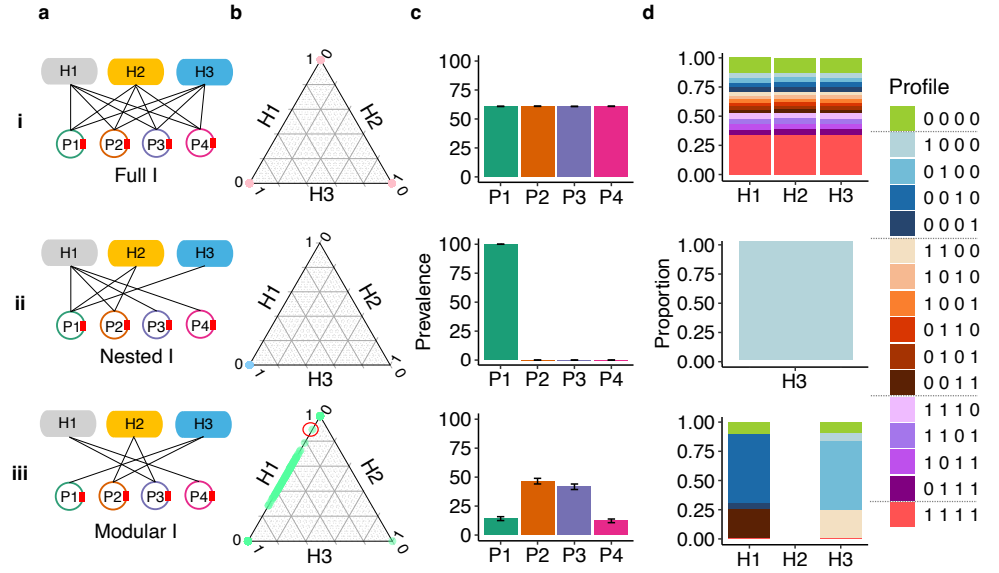


Fig 3. The effect of structure in the infection network **I under a full plasmid compatibility network **P**.** Rows i, ii, and iii represent different **I** structures. (a) Illustration of the structures of **I**. (b) Final relative abundance of host populations. Each dot represents a replicate. Dots on the vertices had no coexistence (i.e. only one population survived), while dots on the edges had coexistence of two populations. For example, the green dot marked with a red circle in b(iii) represents a community with relative abundances of 0.9 for H1, 0.1 for H3, and 0.0 for H2. (c) Mean and SE of final plasmid prevalence across all replicates. (d) Final host population composition, averaged across replicates in which that host population survived (only populations surviving in > 5 replicates were considered). Profiles represent the host subpopulations (e.g., the profile 1000 represents a subpopulation hosting P1). The green dot at $H2 = 1$ in b(iii) is a rare outcome out of 300 simulations.

In contrast, a modular **I** was the only structure that enabled stable host coexistence. The peripheral hosts H1 and H3 were both present at the end of the simulation (coexistence probability of ≈ 0.4) while the bridge host H2 went extinct (coexistence probability ≈ 0) Fig 3b(iii); Figs S4-S6). The rapid extinction of H2 was due to quick co-infection by P2 and P3, which resulted in a higher fitness cost compared to H1 and H3 (Fig S7-S9). The bridge plasmids P2 and P3 had higher final prevalence than the peripheral plasmids P1 and P4 (Fig 3c(iii)). P2 and P3 maintained higher prevalence throughout the simulation because earlier in the simulation when H2 was still present, it acted as a source and increased the rate at which H1 and H3 were infected by these bridge plasmids (Fig S10). The longer-term success of P2 and P3 after their source H2 became extinct is an example of the long-term impact on communities caused by a transient, though unsuccessful population [50].

Combined structures generate non-additive dynamics

Our results so far show that modular networks (especially the infection network) promote the maintenance of diversity. Specifically, we observed prolonged host coexistence with modular **P**, and stable host coexistence with modular **I**. Communities with such structures may therefore be more likely to produce evolutionary innovation.

However, we have only explored structured **I** or **P** separately, while maintaining the other as a fully-connected control. In natural communities, structures likely exist in both of these networks simultaneously, so we next explored the interplay between the two.

Due to the system's non-linearity, it is not straightforward to anticipate how combinations of structures in both networks will interact, or whether their joint effects can be inferred from each network in isolation. Yet we did find a clear case from all the combinations where the two structures counteracted each other's expected influence. Under a modular **I** combined with a hub **P**, the hub plasmid—i.e., the plasmid compatible with all others—did not become the most prevalent, contrary to expectation (Fig 4a; see Figs S1, S4, and S10 for additional combinations). Under a fully connected **I**, the hub plasmid P1 indeed reached fixation in hosts because all hosts became co-infected with P1 (Fig 2c(iii)). However, when **I** was modular, P1 ended with very low average prevalence, whereas P3 reached the highest average prevalence (Fig 4c).

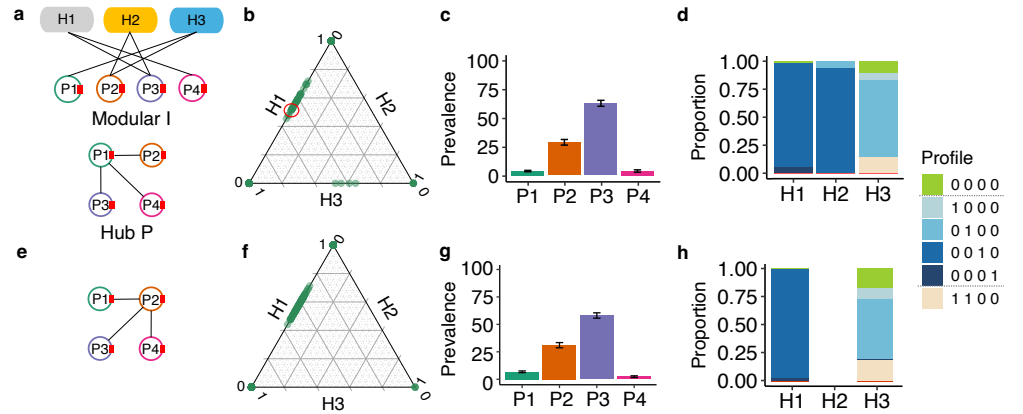


Fig 4. The joint effect of structured networks: modular **I and hub **P**.** (a) The modular network structure of infection **I** and the hub network structure of plasmid compatibility **P** with P1 as the hub plasmid. (b) Final relative abundance of host populations. Each dot represents a replicate. Dots on the vertices had no coexistence (i.e., only one population survives), while dots on the edges had the coexistence of two populations. For example, the green dot marked with a red circle represents a community with relative abundances of 0.5 for H1, 0.5 for H3, and 0.0 for H2. (c) Mean and SE of final plasmid prevalence across all replicates. (d) Final host population composition, averaged across replicates in which that host population survived (only populations surviving in > 5 replicates were considered). (e) Choosing an alternative hub **P** (P2, in the bridge module of the infection network, with a broader host range than P1) resulted in similar (f) final relative host abundance, (g) plasmid prevalence, and (h) host composition. Profiles represent the host subpopulations (e.g., the profile 1000 represents a subpopulation hosting P1).

These patterns resulted from the interaction between the structures of **I** and **P**: although the hub plasmid P1 was compatible with the other three plasmids, the peripheral host H3 was its only possible host (Fig 4a). H3 could therefore be co-infected by P1 and P2. Under a full **P**, the other peripheral host H1 could also be co-infected, but under a hub **P** this was no longer possible. This structure combination led to a higher net fitness of H1 compared to H3 (Fig 4b, d; Fig S9). In addition, while under full **P** H2 always went extinct (Fig 3b(iii)), under structured **P** it coexisted with host H3 in some simulations (Fig 4b). This is because under structured **P** H2 was not susceptible to the burden of co-infection (Fig S9). Importantly, those patterns remain

consistent regardless of the choice of the hub plasmid (Fig 4e-h). Overall, these results suggest that the infection network can counteract the effects of the plasmid compatibility network, especially when both are structured.

Plasmid cost interacts with network structure

Until now, we have assumed a moderate plasmid cost ($c_\alpha = 0.3$), corresponding to a 30% reduction in host growth rate relative to plasmid-free hosts. This choice reflects empirical estimates and acknowledges that plasmid cost directly affects host fitness, potentially leading to the exclusion and extinction of particular host populations [17, 51, 52, 53]. Because compatibility determines whether plasmids can co-reside, it can further amplify or mitigate these fitness effects through their aggregate (here, multiplicative) impact on host growth. Network structure therefore shapes the distribution of fitness differences among hosts, influencing coexistence and associated community-level patterns. We hypothesize that plasmid cost modulates the influence of network structure on community dynamics. When plasmid carriage is moderately costly, growth penalties should interact with host position in the infection network, amplifying or dampening structural differences and limiting how far plasmids can spread through the host community [34]. In contrast, when plasmid costs are negligible or extreme, fitness effects should dominate dynamics, reducing the influence of network structure and weakening its impact on host coexistence and plasmid prevalence.

To test this hypothesis, we systematically varied plasmid cost in our simulations and examined how its interaction with network structure shaped host coexistence, plasmid prevalence, and the distribution of plasmid-free subpopulations. As predicted, the absence of plasmid cost or when plasmid cost is high ($c_\alpha > 0.3$) diminishes the effects of network structures on host coexistence. Specifically, when the compatibility network is structured, hosts coexist for longer under moderate cost compared to no cost or high cost, and this effect is stronger when the infection network is modular (Fig 5, Fig S11), and homogenizes the host survival probability at ca. 1/3 (Fig S12). The absence of plasmid cost reduces the impact of the network on hosts by reducing the burden associated with being exposed to a plasmid, whereas increasing plasmid cost results in intra-specific competition eliminating plasmids by purifying selection, which again reduces the potential for network effects on host dynamics (Figs S13, S14).

Applying the model to an empirical system with heterogeneous parameters

A key simplifying assumption of our model thus far is that hosts and plasmids differ only in their position within the interaction networks. We relaxed this assumption by parameterizing the model using an experimental system, thereby introducing heterogeneity in biological parameters and increasing the biological realism of the dynamics. **Importantly, our aim was not to empirically validate the model**, as such validation would require independent experimental manipulation of infection and compatibility network structures, which is currently not feasible.

We used data reported in [54], comprising three bacterial host populations and two plasmids distinguishable by their colony phenotypes. The size of this empirical system was constrained by the availability of fluorescent labels used to track the plasmids. The community consisted of *Pseudomonas fluorescens* SBW25 (bacterial host H1), *Pseudomonas putida* KT2440 (H2), and *Escherichia coli* MG1655 (H3). The plasmids were the *Pseudomonas*-specific, mercury-resistant plasmid pQBR57 (P1), and the antibiotic-resistant plasmid pKJK5 (P2), which under the experimental conditions was unable to conjugate into *P. fluorescens* SBW25. The system therefore is characterized by a modular **I** and a full **P** (Fig 6a). Because this empirical system only permits a

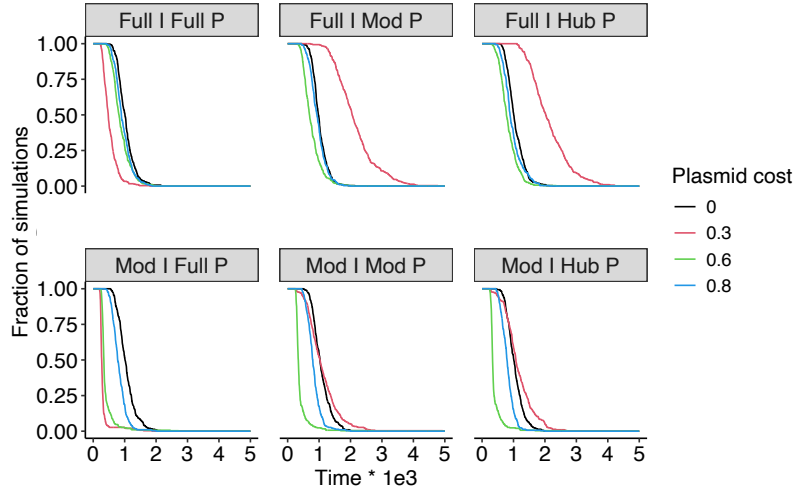


Fig 5. Dynamics of microbe coexistence of three populations across plasmid costs under full infection structures (top row) and modular infection structures (bottom row). The dynamics of coexistence probability (fraction of simulations) is calculated as the proportion of replicates with complete(3-population) coexistence out of total number of replicates across time. Time was only plotted to $t = 5000$ where most probabilities had dropped to zero.

modular infection structure, we do not have empirical data from the unstructured infection network.

We re-parameterized our model using experimental measurements (Table S1-S4). Specifically, we incorporated unequal population growth rates ($H1 \leq H2 < H3$), infection rates ($H1 = H2 < H3$), and plasmid costs ($P1 < P2$), and a heterogeneous interspecific competition network ($H1 < H2 < H3$). For computational tractability, we used lower values of community-wide carrying capacity ($K_{model} = 10^5$ vs $K_{empirical} = 10^9$) and initial abundances ($B_{0model} = 3.3 \times 10^3$ vs $B_{0empirical} = 3.3 \times 10^5$ for each population). These scaling differences did not affect the qualitative outcomes, and we therefore compared empirical and model results in relative terms.

We then compared model outcomes to the empirical dynamics. Following Fig. 3(iii), we expected that in the experimental system the bridge host H2 would be outcompeted by the peripheral hosts and go extinct, and that the resulting community would be primarily composed of infected subpopulations. In contrast to this prediction, H2 maintained a higher relative abundance than the peripheral host H1 (Fig 6b). The most abundant plasmid in the system was P2, mirroring the high abundance of its primary host (Fig 6c). This discrepancy between theoretical expectations and experimental observations can be explained by the heterogeneous growth rates, the interspecific competition network, and an elevated growth rate of the bridge host. We therefore extended the parameterization to explicitly incorporate these factors. When included (Table S1), the simulations qualitatively reproduced the experimental results (Fig 6b-e; Fig S15). These results highlight the influence of trait heterogeneity on the consequences of network structure, underscoring that network effects are contingent on underlying parameter configurations. Exploring how parameter heterogeneity interacts with assumed network structures is therefore an important direction for future work.

Having recapitulated the empirical results with our re-parameterized model, we were then in a position to test our hypothesis using a model that fully relaxes the assumption of uniform trait distributions. We reran the model with an unstructured infection network (full I; Fig 6f). While the host population dynamics remained unchanged

(Fig 6g), the subpopulation dynamics were qualitatively different. Specifically, the less costly plasmid P1 reached a higher community-wide prevalence instead of P2 (Fig 6h vs Fig 6e). These results reinforce our purely theoretical findings, demonstrating that infection network structure can alter plasmid prevalence even in the presence of substantial biological heterogeneity.

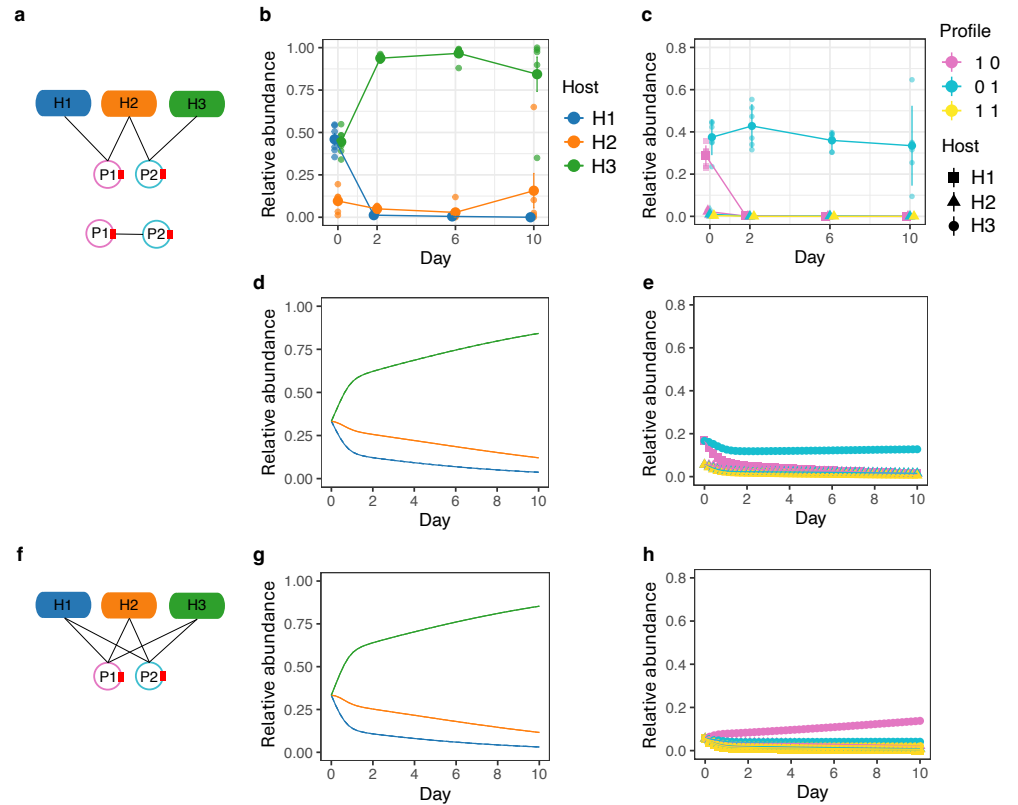


Fig 6. Empirical network structures and simulated population dynamics. (a) Empirical infection network **I** (top) and plasmid compatibility network **P** (bottom) from the empirical system. (b) Host population dynamics in the empirical system. (c) Infected subpopulation (plasmid) dynamics in the empirical system. (d) Simulated host population dynamics using the empirical networks. (e) Simulated infected subpopulation dynamics using the empirical networks. The empirical and modeling systems show similar patterns for host (panel b vs panel d) and plasmid (panel c vs panel e) dynamics. (f) Full infection network **I** used in simulation. (g) Simulated host population dynamics under the full infection network. (h) Simulated infected subpopulation dynamics under the full infection network. All abundances are relative to community size. Error bars represent SE. The empirical observations had a sample size of 6, while the model simulations had a sample size of 300.

Discussion

Although ecological networks are known to shape community dynamics, we still know surprisingly little about how network structures operate in real host–plasmid systems [23, 26]. Empirical data on infection networks and plasmid–plasmid compatibility networks at a community level remain scarce despite increasing studies of plasmid host ranges and co-infection dynamics. Therefore, the effects of each of those networks, let

alone their combination, remain unknown. This work provides a first step toward filling this gap by offering a mechanistic framework for studying how network structure can drive community dynamics. Indeed, our results highlight how the individual and combined effects of host-plasmid infection and plasmid-plasmid compatibility networks determine microbial coexistence and plasmid prevalence, potentially shaping long-term evolutionary trajectories by modulating the effects of selective pressures in the community. Because modeling generates testable hypotheses and highlights the processes most worth measuring, these results can help guide empirical studies toward the interaction patterns most likely to influence plasmid spread and evolutionary potential. Emerging technologies, such as Hi-C [55], can now map these interaction networks at scale, making such targeted investigations increasingly feasible.

A central insight from our work is that the infection network exerts a stronger influence on community dynamics because it is a primary barrier to plasmid-plasmid interaction, generating marked heterogeneity in plasmid prevalence and co-infection patterns across hosts. This asymmetry arises because infection structure determines whether hosts incur plasmid-associated costs at all: hosts that are weakly connected or disconnected in the infection network can avoid plasmid carriage entirely, whereas compatibility structure can only limit additional costs once at least one plasmid is present. Preventing infection is therefore more effective at minimizing fitness costs than restricting co-infection, causing infection structure to act as a first-order filter on plasmid presence and setting an upper bound on the impact of compatibility structure on community dynamics. However, this influence does not operate in isolation: the infection network better maintains its modular structure when the plasmid compatibility network is also structured, revealing that compatibility constraints feed back onto how infection patterns unfold. Structured compatibility also reshapes host population composition and therefore determines where plasmids can co-reside. Such structure–dynamics feedback can affect opportunities for recombination, evolutionary innovation, and the potential emergence of multidrug resistance through horizontal gene transfer among co-infecting plasmids [3, 18, 56, 57]. These model-derived insights are consistent with empirical studies showing that host–plasmid dynamics are governed jointly by direct host interactions and compatibility constraints [22, 46, 53, 58, 59, 60] and that structured infection networks were found to co-occur with restricted plasmid transfer pathways, limiting the spread of costly plasmids [26]. Taken together, these results underscore the importance of studying multiple, coupled networks when seeking to understand the ecological and evolutionary consequences of infectious MGEs.

Our results further indicate a clear asymmetry between host and plasmid dynamics: plasmids are far more likely to persist than their hosts under alternative network structures, provided they can maintain themselves in just one surviving host population. In other words, whereas there can really only be one successful host owing to niche overlap, multiple plasmids can survive in that successful host. This asymmetry emerges because shifts in plasmid compatibility can impose high infection burdens that drive hosts to extinction, whereas changes in infection patterns rarely eliminate plasmids outright as long as any suitable host remains. Consequently, plasmids retain substantial potential for persistence, evolution, and host-range expansion even under reduced host diversity, consistent with empirical observations of broad-host-range plasmids [61].

Plasmid interactions via epistasis (non-additive cost), which is constrained by the compatibility structure, can also affect dynamics. While our model implemented a slight positive epistasis among plasmid costs, a stronger positive epistasis could hinder host coexistence but enhance plasmid co-infection: when the joint cost of carrying multiple plasmids is alleviated, hosts grow faster and compete more strongly within the community, while plasmids coexist more readily within the same host, increasing opportunities for recombination and horizontal transfer. A pure additive effect of

plasmid co-infection, on the other hand, will hinder both host coexistence and plasmid persistence, for co-infected host subpopulations will quickly be out-competed.

In contrast to plasmid compatibility networks, infection networks in our model were inherently unstable, frequently leading to host extinction—even though transient, ultimately unsuccessful host populations could still shape the long-term dynamics of plasmid persistence. This contrasts with natural systems, where modular and nested structures are commonly observed [35, 38, 62], suggesting stabilizing factors for the network structures. Population-level trait heterogeneity and positive epistasis in plasmid fitness costs [8, 17], among other possible factors, may mitigate destabilization, allowing structured networks to persist in nature.

Ideally, theoretical predictions should be evaluated through direct empirical tests. In our case, this would require independent experimental manipulation of infection and compatibility network structures while holding host and plasmid traits constant. This is a technical challenge that would likely require engineered systems. To our knowledge, no current empirical system allows such manipulation of infection networks, making this an important but currently inaccessible direction that we can only address indirectly through simulation. As an intermediate step, we applied our model to a well-characterized experimental system comprising three bacterial hosts and two plasmids forming a modular infection network [54]. Rather than serving as a formal validation, this approach assessed whether incorporating empirically observed network structure is necessary to capture observed dynamics. The dependence of model behavior on the imposed infection structure provides preliminary empirical support for the role of network organization in shaping host–plasmid dynamics, while illustrating how empirically informed models can be used to explore counterfactual network configurations that are not yet experimentally accessible.

Our study focused on a small and fixed system to isolate effects related to network structure, to more easily dissect patterns among populations and subpopulations, and to clarify causal effects among interactions within networks. With this foundation, the model can be expanded to represent larger and more complex bipartite communities. In larger systems, functional redundancy and increased complexity of interactions, resource specialization and trade-offs could dampen the effects of network interplay [63, 64, 65, 66]. An important future research direction is the empirical assembly of infection and compatibility networks, as has been achieved for bacteria–phage systems [35, 40]. Although such network-level data remain rare [26], several studies—particularly those quantifying host ranges [67, 68]—demonstrate promising progress toward reconstructing host–plasmid infection networks, a trend likely to accelerate with emerging technologies such as Hi-C. In contrast, assembling plasmid–plasmid compatibility networks poses a greater challenge, as it requires either identifying the molecular mechanisms that permit or prevent plasmid co-residence, or conducting extensive co-infection experiments across multiple plasmid combinations.

We further assumed uniform and fixed host traits to focus on the effect of network niche (node position). However, incorporating host and plasmid heterogeneity or evolution could alter our predictions [24, 69]. Nevertheless, parameterizing our model according to empirical data did not qualitatively change the key result that structure alters plasmid dynamics. Finally, we did not consider beneficial accessory genes (e.g., antibiotic resistance), which—as shown in an empirical experiment [54]—can shift host–MGE interactions from antagonistic to mutualistic. While this allowed us to generate a theory that is generally relevant for infectious agents, future research could integrate eco-evolutionary feedback and beneficial accessory genes to capture these dynamical aspects of host–plasmid communities.

An open question in microbial ecology is how network structure evolves and persists. While the infection and compatibility networks we modeled resemble those observed in

microbial ecosystems [12, 35, 36, 70, 71, 72, 73], we effectively treated them as boundary conditions within which new links cannot emerge and nodes themselves cannot evolve. In reality, network structures emerge via eco-evolutionary processes [12, 23, 38], and host adaptation, immunity, and plasmid evolution likely result in host-specific fitness effects [53] and shape infection network structure [23, 36]. Plasmid compatibility networks, although much less studied, likely evolve through recombination that reorganizes their replication-partition systems [3] and mutations that modulate incompatibility functions [48]. Adaptive defense mechanisms that mediate plasmid competition [21, 22] may also influence compatibility constraints. Moreover, there may be interacting evolutionary trajectories of the interacting networks, leading to multi-level selection. Future models could incorporate such evolutionary feedback, shifting from fixed boundary conditions to dynamic, emergent structures.

Conclusion

In conclusion, our study provides a novel perspective on microbial ecology by explicitly demonstrating that the interplay between host-plasmid infection and plasmid-plasmid compatibility networks profoundly shapes community dynamics and evolutionary potential. We find that the interconnectedness of these ecological networks itself stabilizes host-plasmid communities and alters their dynamics, underscoring the need to move beyond studying interaction types in isolation. Beyond microbial ecology, these theoretical and modeling developments offer insights into community dynamics of infectious agents and their hosts.

Materials and methods

Host-plasmid model

ODE-based models have been widely used to study host-plasmid dynamics [7, 8, 9], but they are less suited to the specific questions we address here. Our focus is on subpopulation-level dynamics, explicit representation of hosts carrying different plasmids, and incorporating demographic stochasticity [74]. It is also more straightforward to embed heterogeneous network structures within an agent-based model. For these reasons, we use a stochastic agent-based model that captures subpopulation dynamics while allowing the network structures to be represented directly. Below are the overview (entities, spatial and temporal scales), design (events, simulation) and detail (interaction networks, host and plasmid traits, infection propensity, rates, and model limitations) [75].

Entities

The entities of the model were host subpopulations. Each subpopulation of host i contained a plasmid profile p . Each plasmid profile was a vector of elements 0 and 1, representing the presence (1) or absence (0) of each plasmid in the subpopulation. Therefore, a community with n_b hosts and n_p plasmids had at most $n_b \times 2^{n_p}$ subpopulations. We defined $H_{i,p}$ as the abundance of a subpopulation, and H_i as the abundance of host i ($H_i = \sum_{p=\mathbf{0}}^{2^{n_p}-1} H_{i,p}$). For simplicity, we assumed each plasmid had a single copy in each host individual. We present an example for this notation in Table 1. Based on the plasmid profiles, we generated a list of donors (the plasmid-infected subpopulations that can transmit plasmids to others), and for each donor a list of recipients (the subpopulations that can receive plasmids from the donor) during model initialization. The lists of donors and recipients were used to sample subpopulations

that undergo HGT and were updated during the simulations when new subpopulations emerged.

Table 1. Example of entity notation. In this example there are hosts (H1 and H2) and two plasmids (P1 and P2).

Host (i)	Plasmid profile (p)	Abundance ($H_{i,p}$)
1	[0,0]	10
1	[1,0]	5
1	[0,1]	0
1	[1,1]	0
2	[0,0]	10
2	[1,0]	5
2	[0,1]	0
2	[1,1]	0

Spatial and temporal scales

We did not consider a spatial structure. We used hour as the time unit, as most per-capita rates are quantified with this unit in microbial studies. We used a 20000 hours time span for the simulations of the theoretical part to ensure stable coexistence, and a 240 hours (10 days) time span for simulations supporting the lab experiment, which is ample for most host populations/communities to reach carrying capacity in a lab environment [10].

Events

Five major events contributed to the dynamics of the entities: death (D), growth (G), segregation (S), competition (C), and infection (I) (Fig 1b). In each death and competition event, the chosen entity decreased its abundance by one. In each growth event, the chosen entity increased its abundance by one. In each segregation event (i.e., growth with segregation error), we assumed plasmid segregation fails, so the plasmid-free entity $H_{i,0}$ increased its abundance by one. By doing so, we assumed a cell division might lose all rather than one of its plasmid, to keep simulation tractable. Relaxing this assumption will not affect the results, for we also assumed the segregation event occurs very rarely, making its influence negligible. With each infection event, the chosen donor entity $H_{i,p}$ infected a recipient entity $H_{k,q}$, turning it into a transconjugant entity $H_{k,r}$. As a result, the donor's abundance remained the same, the recipient's abundance decreased by one, and the transconjugant's abundance increased by one.

Simulations

We applied the Gillespie algorithm, which includes the following steps:

1. Initialize the system with variable inputs (including parameter values and initial subpopulation abundances) (S1 Appendix and Table S6), and set time t to zero.
2. Calculate the total rate of the system $R = R_D + R_G + R_S + R_C + R_I$, which is composed of the total rates of death (see "Rates" for per-capita rates):

$$R_D = \sum_{i,p} \mu_{i,p} H_{i,p}, \quad (1)$$

growth:

$$R_G = \sum_{i,p} \eta_{i,p} H_{i,p}, \quad (2)$$

segregation:

$$R_S = \sum_{i,p} \omega_{i,p} H_{i,p}, \quad (3)$$

competition:

$$R_C = \sum_{i,p} \xi_{i,p} H_{i,p}, \quad (4)$$

and infection:

$$R_I = \sum_{i,p} \phi_{i,p} H_{i,p} \quad (5)$$

3. Sample the length of a time step $\Delta t = \frac{X}{R}$, where X was drawn from an exponential distribution with a mean of 1.
4. Randomly sample an event, with weights proportional to the event's weight out of the total rate ($R_D/R, R_G/R, R_S/R, R_C/R, R_I/R$).
5. Sample the entity. If the chosen event is not infection, randomly sample an entity $H_{i,p}$, with weights according to the subpopulations' event rates. If the chosen event is infection, first sample a donor entity $H_{i,p}$ from the plasmid-infected subpopulations, with weights according to their infection rates. Then, sample a recipient entity $H_{k,q}$ from the recipient subpopulations that are vulnerable to the donor, with weights according to their abundances. Finally, sample a transconjugant entity $H_{k,r}$, with weights according to the propensity tensor $\mathbf{\Gamma}$ (see "Infection propensity").
6. Execute the chosen event for the chosen entity, and update the simulation time ($t' = t + \Delta t$).
7. Move to step 3 until the simulation time meets the final time. Meanwhile, record the subpopulation abundances when t is equal to or passes desired length of time set for recording the system's set (5 hours in our case).
8. When the simulation reaches the defined time limit $t = 20000$ or t at which the system collapses (all host populations have zero abundance), write the data frame into the output file in SQLite format (S1 Appendix). The output file was used for further analyses.

Interaction networks

We used an infection network and a plasmid compatibility network. The infection network \mathbf{I} was a binary incidence matrix (Fig 7a) that determined if the plasmid β (column) can infect the host i (row). The plasmid compatibility network \mathbf{P} was a symmetric binary matrix (Fig 7b) that determined if two plasmids α and β can coexist within the entity's individuals, with the assumption that plasmids were self-incompatible ($P_{\alpha\beta} = 0 \forall \alpha = \beta$). We also assumed that the hosts had equal strength of interspecific competition for a common resource, and that HGT occurred both between and within hosts.

Host and plasmid traits

For the host, we used per capita growth rate η_i , per capita death rate μ_i , and probability of segregation error e_i . For the plasmids, we used plasmid cost on host growth c_α . We applied a community-wide carrying capacity K , limiting the sum of population abundances. A complete list of parameters and their values is provided in Table 2.

Table 2. Parameter values used in the simulations of the theoretical part. Parameter values were based on/taken from [76].

Host traits	H1	H2	H3	
growth rate η_i	1	1	1	
death rate μ_i	0.12	0.12	0.12	
infection rate γ_i	10^{-5}	10^{-5}	10^{-5}	
segregation rate γ_i	10^{-8}	10^{-8}	10^{-8}	
community-wide carrying capacity K	20000	20000	20000	
intraspecific competition coefficient a_{ii}	1	1	1	
interspecific competition coefficient a_{ij}	0.01	0.01	0.01	
Plasmid traits	P1	P2	P3	P4
plasmid cost c_α	0.3	0.3	0.3	0.3

Infection propensity

When the infection event is chosen, we considered the propensities with which transconjugants were generated given combinations of donors and recipients. Specifically, we used a three-dimensional infection propensity tensor $\mathbf{\Gamma}$, with each dimension of size $n_b^{n_p}$ corresponding to all potential entities (subpopulations) $H_{i,p}$ along the transconjugant, donor, and recipient axes. We assumed that the more plasmids transmitted in an infection, the lower the propensity. Thus, the elements (propensities) of $\mathbf{\Gamma}$ that met the infection conditions (Table 3) were estimated following the power law:

$$\Gamma_{k,r;i,p;k,q} = \frac{1}{2^{\nu-1}}, \quad (6)$$

Here, $\Gamma_{k,r;i,p;k,q}$ represented the propensity of the recipient $H_{k,q}$, after receiving plasmid(s) from donor $H_{i,p}$, to become transconjugant $B_{k,r}$. The parameter ν represented the number of plasmid strains being transferred from the donor to the recipient. Other elements of $\mathbf{\Gamma}$ were treated as 0. We provide an example propensity tensor for a system with one host and two plasmids in Fig 7c.

Table 3. Conditions for infection to occur.

Condition	Content
1	Donor is plasmid-infected ($p \neq \mathbf{0}$)
2	Donor has plasmid(s) that the recipient does not
3	Transferable plasmid(s) can infect the recipient ($\mathbf{I}_{\beta i} = 1$)
4	Plasmids in the transconjugant can coexist ($\mathbf{P}_{\alpha\beta} = 1$)

Rates

The dynamics of the subpopulations (S1 Appendix and Fig S16) were based on a modified Lotka-Volterra model with infection-recovery elements and direct competition

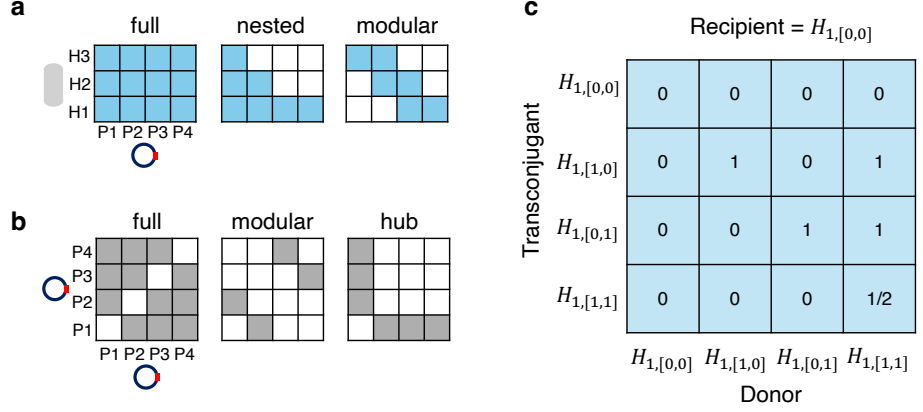


Fig 7. The (a) infection network structures I and (b) plasmid compatibility network structures P represented as matrices. (c) An example of a propensity tensor. Colored blocks in (a) and (b) represent blocks with value 0, while white blocks represent blocks with value 1. Quantified structural characteristics of these networks are further displayed in Table S8 and Table S9. The propensity tensor example focuses on the dimension of the recipient $H_{k=1,q=[0,0]}$. Element $\Gamma_{1,[1,1];1,[1,1];1,[0,0]} = 1/2$ because there are two plasmids being transferred from the donor $H_{i=1,p=[1,1]}$ to the recipient $H_{k=1,q=[0,0]}$, creating the transconjugant $H_{k=1,r=[1,1]}$. Each column of the propensity tensor (i.e., with a given combination of donor and recipient) with at least one element > 0 was then normalized to 1, ensuring the propensities of each column summed up to 1.

events (individuals killing each other due to competition over a common resource; see S1 Appendix and Figs S17-20 for results from indirect competition, i.e., density-dependent growth). In this model, each subpopulation had its per capita rate of events based on strain and plasmid profile, and its total rates of events based on its per capita rates \times abundance, which summed up to the total rate of events R . Below we define the equations of subpopulation per capita rates (variables used in the equations are described in Table S5). We defined the subpopulation per capita death rate as $\mu_{i,p} = \mu_i$ (host-specific) and the per capita growth rate as

$$\eta_{i,p} = \eta_i \prod_{\alpha | p_{\alpha} \neq 0} (1 - c_{\alpha}), \quad (7)$$

where the realized growth rate was the host-specific per capita growth rate, η_i , times the product of the complements of the costs across plasmids hosted by the subpopulation. Therefore, we assumed that the plasmid costs are not additive but multiplicative for the host, resulting in a slight positive epistasis (as the cost of each plasmid is smaller than 1, the multiplicative cost will be smaller than the pure additive cost). We defined the subpopulation per capita segregation rate as

$$\omega_{i,p} = e_i \eta_{i,p}. \quad (8)$$

We defined the competition matrix \mathbf{A} , in which each cell a_{ij} is the effect of host j on the per-capita growth rate of host i . As with other parameters, we used a uniform $a_{ij} = 0.01$ to ensure that the community effects we get are not due to some random competitive advantage of one host over another, but rather due to the structure of the

networks. We applied a community-wide carrying capacity K , and defined the subpopulation per capita competition rate as

$$\xi_{i,p} = \eta_{i,p} \left(\sum_j b_{ij} \frac{H_j}{K} \right). \quad (9)$$

Here, $b_{ij} = a_{ij} + 1$ for $i \neq j$, and b_{ij} equals to 1 when $i = j$.

We defined the subpopulation per capita infection rate $\phi_{i,p}$ as

$$\phi_{i,p} = \gamma_{i,p} \sum H_{i,p} \in \mathbf{L}, \quad (10)$$

where $\gamma_{i,p}$ is the per capita encounter rate between a donor (i.e., plasmid-hosting) and its recipients, and was either host-specific for subpopulations hosting plasmid(s), or zero for the plasmid-free subpopulations. \mathbf{L} was the set of recipient subpopulations that could receive plasmid(s) from the donor subpopulation. While the mechanisms by which the donors and recipients of plasmids meet could be complex [77], we assumed these mechanisms to be donor-dependent and plasmid-profile-independent.

Model limitations

Although our model can simulate multihost–multiplasmid systems, it faces computational constraints as system complexity increases. As the number of host (n_b) and plasmid populations (n_p) increases, so does the time required to generate the infection propensity tensor (of size $n_b \times 2^{n_p}$ in each of the three dimensions), and to initialize the system (e.g., generate lists of donors and corresponding recipients) unless the interaction networks are extremely sparse. Because the Gillespie algorithm is used, increasing system complexity and community-wide carrying capacity inevitably raises the total event rate R . This, in turn, reduces the sampled time step in each iteration, making it more time-consuming for the simulation to reach the final time (S1 Appendix and Fig S21).

Experimental design

We used a 3×3 factorial design of the combinations of \mathbf{I} and \mathbf{P} , which resulted in 9 experiments (Table 4). Due to the stochastic nature of the model, we ran 300 replicates for each experiment, each with a different seed for random sampling. To test how plasmids spread, we initiated populations with a low abundance of monoplasmidic subpopulations (10) compared to plasmid-free subpopulations (2000). We included all potential monoplasmidic subpopulations, so that each plasmid already existed in focal hosts before it was acquired from other hosts.

For the empirical observation, the host-plasmid communities were cultured over five 48-hour transfers (10 days) in shaken liquid medium. We used the empirical data only from the communities that did not experience environmental stress. We used bacterial derivatives and fluorescent proteins to track different host populations and plasmids, and applied a link-balanced initial community composition, where all populations started with equal abundance, comprising of 50% plasmid-free subpopulation and 50% plasmid-carrying subpopulations. We quantified population and subpopulation abundance on days 2, 6, and 10, and summarized population and subpopulation dynamics.

Code and data availability

The code and data for model simulation, input generation, output analyses, and empirical data analysis is available in the dedicated Github repository associated with

Table 4. Experimental design of the theoretical part.

Expt.(code)	I	P
1 (Full I Full P)	full	full
2 (Full I Mod P)	full	modular
3 (Full I Hub P)	full	hub
4 (Nest I Full P)	nested	full
5 (Nest I Mod P)	nested	modular
6 (Nest I Hub P)	nested	hub
7 (Mod I Full P)	modular	full
8 (Mod I Mod P)	modular	modular
9 (Mod I Hub P)	modular	hub

this paper at: https://github.com/HFSP-EcoNets/model_code. Empirical data is also available in the collaborative study by Schaal et al. [54].

Supplementary information

S1 Fig. Relative abundance of populations at the end of the simulations (t = 20000 hours). Dots on the vertices represent no coexistence (i.e. only one population survived), while dots on the edges represent the coexistence of two populations.

S2 Fig. Dynamics of subpopulation abundance (mean \pm 1 SE) at full I x full P. Note that the number of replicates of a subpopulation at a given time point may vary across time, for it depends on how many replicates still have that subpopulation at that time point. The K at y-axis represents carrying capacity. Time was only plotted to t = 3000 where equilibrium of subpopulations had been reached. Note the plasmid-free subpopulation (green line) first increased then decreased.

S3 Fig. Dynamics of subpopulation abundance (mean \pm 1 SE) at nested I x full P. Note that the number of replicates of a subpopulation at a given time point may vary across time, for it depends on how many replicates still have that subpopulation at that time point. The K at y-axis represents carrying capacity. Time was only plotted to t = 3000 where equilibrium of subpopulations had been reached.

S4 Fig. Dynamics of microbe coexistence of three populations (solid line) and two populations (dashed line) at the end of the simulations (t = 20000 hours). The dynamics of coexistence probability (fraction of simulations) is calculated as the proportion of replicates with complete(3-population)/partial(2-population) coexistence out of total number of replicates across time. Time was only plotted to t = 5000 where all probabilities had dropped to zero.

S5 Fig. Dynamics of (a) population abundance and (b) subpopulation abundance at modular I x full P from replicate 21. Replicate 21 demonstrated the stable coexistence scenario where the plasmid-free subpopulations of the peripheral hosts persisted. The K at y-axis represents carrying capacity. Interestingly, populations and subpopulations fluctuated with alternative amplitudes around mean abundance. This is because there was a dynamical balance between primary and secondary plasmid infections between the coexisting hosts.

S6 Fig. Dynamics of (a) population abundance and (b) subpopulation abundance at modular I x full P from replicate 23. Replicate 23 demonstrated the unstable coexistence scenario where the plasmid-free subpopulations of the peripheral hosts went extinct. When the plasmid-free subpopulations went extinct, monoplasmodic subpopulations lost input from infection, and the remaining monoplasmodic individuals quickly got co-infected, destabilizing the oscillatory dynamics of the coexisting populations. The K at y-axis represents carrying capacity. Time was only plotted to $t = 3000$ where equilibrium of subpopulations had been reached.

S7 Fig. Dynamics of subpopulation abundance (mean \pm 1 SE) at modular I x full P. Note that the number of replicates of a subpopulation at a given time point may vary across time, as it depends on how many replicates still have that subpopulation at that time point. The K at y-axis represents carrying capacity. The high abundance of P3-infected H2 is from a rare case (one from 300 replicates).

S8 Fig. Dynamics of subpopulation abundance (mean \pm 1 SE) at modular I x modular P. Note that the number of replicates of a subpopulation at a given time point may vary across time, for it depends on how many replicates still have that subpopulation at that time point. The K at y-axis represents carrying capacity. The subpopulation abundances of H2 are from 65 replicates.

S9 Fig. Dynamics of subpopulation abundance (mean \pm 1 SE) at modular I x hub P. Note that the number of replicates of a subpopulation at a given time point may vary across time, for it depends on how many replicates still have that subpopulation at that time point. The K at y-axis represents carrying capacity. The subpopulation abundances of H2 are from 9 replicates.

S10 Fig. Dynamics of plasmid prevalence (mean \pm 1 SE). Time was only plotted to $t = 10000$ where equilibrium of plasmid prevalence had been reached.

S11 Fig. Dynamics of microbe coexistence of (a) three populations (solid line) and (b) two populations (dashed line) across plasmid costs. The dynamics of coexistence probability (fraction of simulations) is calculated as the proportion of replicates with complete(3-population)/partial(2-population) coexistence out of total number of replicates across time. Time was only plotted to $t = 5000$ where most probabilities had dropped to zero.

S12 Fig. Relative abundance of populations at the end of the simulations ($t = 20000$ hours) when plasmid cost = (a) 0, (b) 0.3, (c) 0.6, and (d) 0.8. Dots on the vertices represent no coexistence (i.e. only one population survived), while dots on the edges represent the coexistence of two populations.

S13 Fig. Mean and SE of final plasmid prevalence across all replicates when plasmid cost = (a) 0, (b) 0.3, (c) 0.6, and (d) 0.8.

S14 Fig. Final host population composition when plasmid cost = (a) 0, (b) 0.3, (c) 0.6, and (d) 0.8., averaged across replicates in which that host population survived (only populations surviving in > 5 replicates were considered). Profiles represent the host subpopulations (e.g., the profile 1000 represents a subpopulation hosting only P1).

S15 Fig. (a) The host population dynamics and (b) host subpopulation dynamics from the simulations assuming no increase on the growth rate of the bridge host H2 under a modular I based on an empirical system (Figure 5a, top row).

S16 Fig. Illustration of the dynamics of plasmid-carrying subpopulation (left box with a circle in it) and plasmid-free subpopulation (right box). Colored arrows indicate abundance inflows/outflows from the five events: growth (green), death (red), competition (purple), infection (orange), and segregation (blue). Alongside each arrow lists the per capita rate of the event, with subscripts denoting host i and plasmid profile p of the subpopulation.

S17 Fig. Dynamics of microbe coexistence of three populations (solid line) and two populations (dashed line) under density-dependent growth. The dynamics of coexistence probability (fraction of simulations) is calculated as the proportion of replicates with complete(3-population)/partial(2-population) coexistence out of total number of replicates across time. Time was only plotted to $t = 5000$ where most probabilities had dropped to zero or stabilized.

S18 Fig. Relative abundance of populations at the end of the simulations ($t = 20000$ hours) under density-dependent growth. Dots on the vertices represent no coexistence (i.e. only one population survived), while dots on the edges represent the coexistence of two populations.

S19 Fig. Mean and SE of final plasmid prevalence across all replicates under density-dependent growth.

S20 Fig. Final host population composition under density-dependent growth, averaged across replicates in which that host population survived (only populations surviving in > 5 replicates were considered). Profiles represent the host subpopulations (e.g., the profile 1000 represents a subpopulation hosting only P1).

S21 Fig. Elapse time of tensor generation, initialization and simulation across system complexity n , i.e. the number of host and plasmid populations in the system.

S1 Appendix. Supporting information for the host-plasmid model. Subpopulation dynamics, input and output, complexity-dependent computational efficiency, and the results from an alternative model with density-dependent growth rate.

S1 Table. Host-specific parameters. The net population growth rates were parameterized using the empirical data fit to the standard form of the logistic equation in the R package *growthcurver* [78], while the population growth rates and death rates were arbitrarily assigned to match the net population growth rate. The infection rates and competition coefficients were assigned in a relative magnitude in order to better match the empirical subpopulation and population dynamics. The segregation rates were fixed to an extremely low value so these can be negligible. The community-wise carrying capacity was arbitrarily assigned for computational efficiency. We later assumed an increase in the growth rate of the bridge host (H2).

S2 Table. Plasmid-specific parameters.	806
The plasmid costs were assigned in a	807
relative magnitude based on empirical monocultures of the infected bridge host	808
population in order to better match the empirical subpopulation and population	809
dynamics. The plasmid resistance to stress was arbitrarily assigned and fixed as these	810
are irrelevant for systems without stress.	
S3 Table. Initial abundance of the plasmid-present system for a modular	811
infection network I.	812
S4 Table. Initial abundance of the plasmid-present system for a full	813
infection network I.	814
S5 Table. Constants and parameters for the model.	815
S6 Table. Variables for the model input.	816
S7 Table. Constants and parameters for the model performance test.	817
S8 Table. Quantified modularity (Q) and nestedness (NODF) of the	818
designed bipartite infection networks I.	819
Q (between 0 and 1 for natural ecological	820
networks) is computed following Barber (2007) [79], while NODF (between 1 and 100)	821
is computed following Almeida-Neto et al. (2008) [80].	
S9 Table. Quantified Modularity (Qmax) and degree heterogeneity (H) of	822
the designed unipartite plasmid compatibility networks P.	823
Qmax (between 0	824
and 1 for natural ecological networks) is computed following Newman and Girvan (2004)	825
[81], while H (between 0 and infinity; with 0.33 for a small network of four nodes	826
indicating a star-like hub structure) is computed following Estrada (2010) [82].	

Acknowledgments

We thank G. Galai for technical support in programming. Prof. David Alonso and Prof. Mercedes Pascual provided insightful comments. The study was funded by the Human Frontier Science Program (grant RGY0064/2022) to S.P., J.P.J.H., M.D.D. Kreitman School of Advanced Graduate Studies, Ben-Gurion University of the Negev, supported the fellowship of Y.J.

References

1. Kornelia S, Jechalke S, Eva M T. Plasmid Detection, Characterization, and Ecology. Microbiology Spectrum. 2015;3(1):10.1128/microbiolspec.plas-0038-2014. doi:10.1128/microbiolspec.plas-0038-2014.
2. San Millan A. Evolution of Plasmid-mediated antibiotic resistance in the clinical context. Trends Microbiol. 2018;26(12):978–985. doi:10.1016/j.tim.2018.06.007.
3. Rodríguez-Beltrán J, DelaFuente J, León-Sampedro R, MacLean RC, San Millán Beyond horizontal gene transfer: the role of plasmids in bacterial evolution. Nat Rev Microbiol. 2021;6:347–359. doi:10.1038/s41579-020-00497-1.

4. San Millan A, MacLean RC. Fitness Costs of Plasmids: a Limit to Plasmid Transmission. *Microbiology Spectrum*. 2017;5(5). doi:10.1128/microbiolspec.mtbp-0016-2017.
5. Hall JPJ, Wright RCT, Harrison E, Muddiman KJ, Wood AJ, Paterson S, et al. Plasmid fitness costs are caused by specific genetic conflicts enabling resolution by compensatory mutation. *PLoS Biol*. 2021;19(10):e3001225. doi:10.1371/journal.pbio.3001225.
6. Ghoul M, Mitri S. The ecology and evolution of microbial competition. *Trends Microbiol*. 2016;24(10):833–845. doi:10.1016/j.tim.2016.06.011.
7. Coyte KZ, Stevenson C, Knight CG, Harrison E, Hall JPJ, Brockhurst MA. Horizontal gene transfer and ecological interactions jointly control microbiome stability. *PLoS Biol*. 2022;20(11):e3001847. doi:10.1371/journal.pbio.3001847.
8. Igler C, Huisman JS, Siedentop B, Bonhoeffer S, Lehtinen S. Plasmid co-infection: linking biological mechanisms to ecological and evolutionary dynamics. *Philos Trans R Soc Lond B Biol Sci*. 2022;377(1842):20200478. doi:10.1098/rstb.2020.0478.
9. Dewan I, Uecker H. A mathematician’s guide to plasmids: an introduction to plasmid biology for modellers. *Microbiology*. 2023;169(7). doi:10.1099/mic.0.001362.
10. Hall JPJ, Jamie Wood A, Harrison E, Brockhurst MA. Source–sink plasmid transfer dynamics maintain gene mobility in soil bacterial communities. *Proc Natl Acad Sci U S A*. 2016;113(29):8260–8265. doi:10.1073/pnas.1600974113.
11. Kottara A, Carrilero L, Harrison E, Hall JPJ, Brockhurst MA. The dilution effect limits plasmid horizontal transmission in multispecies bacterial communities. *Microbiology*. 2021;167(9). doi:10.1099/mic.0.001086.
12. Pilosof S, Alcalá-Corona SA, Wang T, Kim T, Maslov S, Whitaker R, et al. The network structure and eco-evolutionary dynamics of CRISPR-induced immune diversification. *Nat Ecol Evol*. 2020;4:1650–1660. doi:10.1038/s41559-020-01312-z.
13. Alderliesten JB, Duxbury SJN, Zwart MP, de Visser JAGM, Stegeman A, Fischer EAJ. Effect of donor-recipient relatedness on the plasmid conjugation frequency: a meta-analysis. *BMC Microbiol*. 2020;20(1):135. doi:10.1186/s12866-020-01825-4.
14. Deep A, Gu Y, Gao YQ, Ego KM, Herzik MA Jr, Zhou H, et al. The SMC-family Wadjet complex protects bacteria from plasmid transformation by recognition and cleavage of closed-circular DNA. *Mol Cell*. 2022;82(21):4145–4159.e7. doi:10.1016/j.molcel.2022.09.008.
15. Jaskólska M, Adams DW, Blokesch M. Two defence systems eliminate plasmids from seventh pandemic *Vibrio cholerae*. *Nature*. 2022;604(7905):323–329. doi:10.1038/s41586-022-04546-y.
16. Novick RP. Plasmid incompatibility. *Microbiol Rev*. 1987;51(4):381–395. doi:10.1128/mr.51.4.381-395.1987.
17. San Millan A, Heilbron K, MacLean RC. Positive epistasis between co-infecting plasmids promotes plasmid survival in bacterial populations. *ISME J*. 2014;8(3):601–612. doi:10.1038/ismej.2013.182.

18. Dionisio F, Zilhão R, Gama JA. Interactions between plasmids and other mobile genetic elements affect their transmission and persistence. *Plasmid*. 2019;102:29–36. doi:10.1016/j.plasmid.2019.01.003.
19. Cooper TF, Heinemann JA. Postsegregational killing does not increase plasmid stability but acts to mediate the exclusion of competing plasmids. *Proc Natl Acad Sci U S A*. 2000;97(23):12643–12648. doi:10.1073/pnas.220077897.
20. Helinski DR. A Brief History of Plasmids. *EcoSal Plus*. 2022;10(1):eESP00282021. doi:10.1128/ecosalplus.esp-0028-2021.
21. Pinilla-Redondo R, Mayo-Muñoz D, Russel J, Garrett RA, Randau L, Sørensen SJ, et al. Type IV CRISPR-Cas systems are highly diverse and involved in competition between plasmids. *Nucleic Acids Res*. 2020;48(4):2000–2012. doi:10.1093/nar/gkz1197.
22. Rocha EPC, Bikard D. Microbial defenses against mobile genetic elements and viruses: Who defends whom from what? *PLoS Biol*. 2022;20(1):e3001514. doi:10.1371/journal.pbio.3001514.
23. Pilosof S. Conceptualizing microbe–plasmid communities as complex adaptive systems. *Trends in Microbiology*. 2023;doi:10.1016/j.tim.2023.01.007.
24. Zhu S, Hong J, Wang T. Horizontal gene transfer is predicted to overcome the diversity limit of competing microbial species. *Nat Commun*. 2024;15(1):800. doi:10.1038/s41467-024-45154-w.
25. Wang T, You L. The persistence potential of transferable plasmids. *Nat Commun*. 2020;11(1):5589. doi:10.1038/s41467-020-19368-7.
26. Risely A, Newbury A, Stalder T, Simmons BI, Top EM, Buckling A, et al. Host-plasmid network structure in wastewater is linked to antimicrobial resistance genes. *Nat Commun*. 2024;15(1):555. doi:10.1038/s41467-024-44827-w.
27. Bastolla U, Fortuna MA, Pascual-García A, Ferrera A, Luque B, Bascompte J. The architecture of mutualistic networks minimizes competition and increases biodiversity. *Nature*. 2009;458(7241):1018–1020. doi:10.1038/nature07950.
28. Thébault E, Fontaine C. Stability of ecological communities and the architecture of mutualistic and trophic networks. *Science*. 2010;329(5993):853–856. doi:10.1126/science.1188321.
29. Pilosof S, Porter MA, Pascual M, Kéfi S. The multilayer nature of ecological networks. *Nature Ecology and Evolution*. 2017;1(4). doi:10.1038/s41559-017-0101.
30. Pilosof S, He Q, Tiedje KE, Ruybal-Pesántez S, Day KP, Pascual M. Competition for hosts modulates vast antigenic diversity to generate persistent strain structure in *Plasmodium falciparum*. *PLoS Biol*. 2019;17(6). doi:10.1371/journal.pbio.3000336.
31. Liaghat A, Yang J, Whitaker R, Pascual M. Punctuated virus-driven succession generates dynamical alternations in CRISPR-mediated microbe-virus coevolution. *J R Soc Interface*. 2024;21(217):20240195. doi:10.1098/rsif.2024.0195.
32. Coyte KZ, Schluter J, Foster KR. The ecology of the microbiome: Networks, competition, and stability. *Science*. 2015;350(6261):663–666. doi:10.1126/science.aad2602.

33. Li L, Liu Y, Xiao Q, Xiao Z, Meng D, Yang Z, et al. Dissecting the HGT network of carbon metabolic genes in soil-borne microbiota. *Front Microbiol.* 2023;14:1173748. doi:10.3389/fmicb.2023.1173748.
34. Newbury A, Dawson B, Klümper U, Hesse E, Castledine M, Fontaine C, et al. Fitness effects of plasmids shape the structure of bacteria-plasmid interaction networks. *Proc Natl Acad Sci U S A.* 2022;119(22):e2118361119. doi:10.1073/pnas.2118361119.
35. Flores CO, Meyer JR, Valverde S, Farr L, Weitz JS. Statistical structure of host-phage interactions. *Proc Natl Acad Sci U S A.* 2011;108(28):E288–97. doi:10.1073/pnas.1101595108.
36. Weitz JS, Poisot T, Meyer JR, Flores CO, Valverde S, Sullivan MB, et al. Phage-bacteria infection networks. *Trends Microbiol.* 2013;21(2):82–91. doi:10.1016/j.tim.2012.11.003.
37. Martiny JBH, Riemann L, Marston MF, Middelboe M. Antagonistic coevolution of marine planktonic viruses and their hosts. *Ann Rev Mar Sci.* 2014;6(1):393–414. doi:10.1146/annurev-marine-010213-135108.
38. Beckett SJ, Williams HTP. Coevolutionary diversification creates nested-modular structure in phage-bacteria interaction networks. *Interface Focus.* 2013;3(6):20130033. doi:10.1098/rsfs.2013.0033.
39. Fortuna MA, Barbour MA, Zaman L, Hall AR, Buckling A, Bascompte J. Coevolutionary dynamics shape the structure of bacteria-phage infection networks. *Evolution.* 2019;73(5):1001–1011. doi:10.1111/evo.13731.
40. Popa O, Dagan T. Trends and barriers to lateral gene transfer in prokaryotes. *Curr Opin Microbiol.* 2011;14(5):615–623. doi:10.1016/j.mib.2011.07.027.
41. Popa O, Landan G, Dagan T. Phylogenomic networks reveal limited phylogenetic range of lateral gene transfer by transduction. *ISME J.* 2017;11(2):543–554. doi:10.1038/ismej.2016.116.
42. Smillie C, Garcillán-Barcia MP, Francia MV, Rocha EPC, de la Cruz F. Mobility of plasmids. *Microbiol Mol Biol Rev.* 2010;74(3):434–452. doi:10.1128/MMBR.00020-10.
43. Jiang W, Maniv I, Arain F, Wang Y, Levin BR, Marraffini LA. Dealing with the evolutionary downside of CRISPR immunity: bacteria and beneficial plasmids. *PLoS Genet.* 2013;9(9):e1003844. doi:10.1371/journal.pgen.1003844.
44. Fraikin N, Couturier A, Lesterlin C. The winding journey of conjugative plasmids toward a novel host cell. *Curr Opin Microbiol.* 2024;78(102449):102449. doi:10.1016/j.mib.2024.102449.
45. Sota M, Yano H, Hughes JM, Daughdrill GW, Abdo Z, Forney LJ, et al. Shifts in the host range of a promiscuous plasmid through parallel evolution of its replication initiation protein. *ISME J.* 2010;4(12):1568–1580. doi:10.1038/ismej.2010.72.
46. Gama JA, Zilhão R, Dionisio F. Plasmid Interactions Can Improve Plasmid Persistence in Bacterial Populations. *Front Microbiol.* 2020;11:2033. doi:10.3389/fmicb.2020.02033.

47. Ślesak W, Jedryszek P, Cazares D, Matlock W, MacLean RC. Plasmids link antibiotic resistance genes and phage defense systems in *E. coli*. bioRxiv. 2025;doi:10.1101/2025.07.25.666796.
48. Santos-Lopez A, Bernabe-Balas C, Ares-Arroyo M, Ortega-Huedo R, Hoefer A, San Millan A, et al. A naturally occurring single nucleotide polymorphism in a multicopy Plasmid produces a reversible increase in antibiotic resistance. *Antimicrob Agents Chemother*. 2017;61(2):AAC.01735–16. doi:10.1128/AAC.01735-16.
49. Haegeman B, Etienne RS. Relaxing the zero-sum assumption in neutral biodiversity theory. *J Theor Biol*. 2008;252(2):288–294. doi:10.1016/j.jtbi.2008.01.023.
50. Amor DR, Ratzke C, Gore J. Transient invaders can induce shifts between alternative stable states of microbial communities. *Sci Adv*. 2020;6(8):eaay8676. doi:10.1126/sciadv.aay8676.
51. Hall JPJ, Harrison E, Lilley AK, Paterson S, Spiers AJ, Brockhurst MA. Environmentally co-occurring mercury resistance plasmids are genetically and phenotypically diverse and confer variable context-dependent fitness effects. *Environ Microbiol*. 2015;17(12):5008–5022. doi:10.1111/1462-2920.12901.
52. Valle AAd, León-Sampedro R, Rodríguez-Beltrán J, DelaFuente J, Hernández-García M, Ruiz-Garbajosa P, et al. The distribution of plasmid fitness effects explains plasmid persistence in bacterial communities. bioRxiv. 2020;doi:10.1101/2020.08.01.230672.
53. Alonso-Del Valle A, León-Sampedro R, Rodríguez-Beltrán J, DelaFuente J, Hernández-García M, Ruiz-Garbajosa P, et al. Variability of plasmid fitness effects contributes to plasmid persistence in bacterial communities. *Nat Commun*. 2021;12(1):2653. doi:10.1038/s41467-021-22849-y.
54. Schaal KA, Wang YJ, Nauta J, De Domenico M, Pilosof S, Hall JPJ. Species interactions determine plasmid persistence in a 3-member bacterial community. bioRxiv. 2025;doi:10.1101/2025.05.31.657151.
55. Castañeda-Barba S, Ridenhour BJ, Top EM, Stalder T. Detection of rare plasmid hosts using a targeted Hi-C approach. *ISME Commun*. 2025;5(1):ycae161.
56. Lam MMC, Wyres KL, Wick RR, Judd LM, Fostervold A, Holt KE, et al. Convergence of virulence and MDR in a single plasmid vector in MDR *Klebsiella pneumoniae* ST15. *J Antimicrob Chemother*. 2019;74(5):1218–1222. doi:10.1093/jac/dkz028.
57. Wang X, Zhang H, Yu S, Li D, Gillings MR, Ren H, et al. Inter-plasmid transfer of antibiotic resistance genes accelerates antibiotic resistance in bacterial pathogens. *ISME J*. 2024;18(1). doi:10.1093/ismejo/wrad032.
58. Kottara A, Hall JPJ, Harrison E, Brockhurst MA. Variable plasmid fitness effects and mobile genetic element dynamics across *Pseudomonas* species. *FEMS Microbiol Ecol*. 2018;94(1). doi:10.1093/femsec/fix172.
59. Fernández-Calvet A, Toribio-Celestino L, Alonso-Del Valle A, Sastre-Dominguez J, Valdes-Chiara P, San Millan A, et al. The distribution of fitness effects of plasmid pOXA-48 in clinical enterobacteria. *Microbiology*. 2023;169(7). doi:10.1099/mic.0.001369.

60. Gama JA, Zilhão R, Dionisio F. Impact of plasmid interactions with the chromosome and other plasmids on the spread of antibiotic resistance. *Plasmid*. 2018;99:82–88. doi:10.1016/j.plasmid.2018.09.009.
61. Loftie-Eaton W, Yano H, Burleigh S, Simmons RS, Hughes JM, Rogers LM, et al. Evolutionary paths that expand Plasmid host-range: Implications for spread of antibiotic resistance. *Mol Biol Evol*. 2016;33(4):885–897. doi:10.1093/molbev/msv339.
62. Kauffman KM, Chang WK, Brown JM, Hussain FA, Yang J, Polz MF, et al. Resolving the structure of phage-bacteria interactions in the context of natural diversity. *Nat Commun*. 2022;13(1):372. doi:10.1038/s41467-021-27583-z.
63. Biggs CR, Yeager LA, Bolser DG, Bonsell C, Dichiera AM, Hou Z, et al. Does functional redundancy affect ecological stability and resilience? A review and meta-analysis. *Ecosphere*. 2020;11(7). doi:10.1002/ecs2.3184.
64. Wood ZT, Palkovacs EP, Olsen BJ, Kinnison MT. The importance of Eco-evolutionary potential in the anthropocene. *Bioscience*. 2021;71(8):805–819. doi:10.1093/biosci/biab010.
65. Puente-Sánchez F, Pascual-García A, Bastolla U, Pedrós-Alió C, Tamames J. Cross-biome microbial networks reveal functional redundancy and suggest genome reduction through functional complementarity. *Commun Biol*. 2024;7(1):1046. doi:10.1038/s42003-024-06616-5.
66. Wortel MT. Evolutionary coexistence in a fluctuating environment by specialization on resource level. *J Evol Biol*. 2023;36(3):622–631. doi:10.1111/jeb.14158.
67. Klümper U, Riber L, Dechesne A, Sannazzarro A, Hansen LH, Sørensen SJ, et al. Broad host range plasmids can invade an unexpectedly diverse fraction of a soil bacterial community. *ISME J*. 2015;9(4):934–945. doi:10.1038/ismej.2014.191.
68. Robinson CRP, Dolezal AG, Liachko I, Newton ILG. Hi-C-resolved metagenomics reveals host range variation among mobile genetic elements within the European honey bee. *MBio*. 2025;16(11):e0224325. doi:10.1128/mbio.02243-25.
69. Alonso-Del Valle A, Toribio-Celestino L, Quirant A, Pi CT, DelaFuente J, Canton R, et al. Antimicrobial resistance level and conjugation permissiveness shape plasmid distribution in clinical enterobacteria. *Proc Natl Acad Sci U S A*. 2023;120(51):e2314135120. doi:10.1073/pnas.2314135120.
70. Light S, Kraulis P, Elofsson A. Preferential attachment in the evolution of metabolic networks. *BMC Genomics*. 2005;6(1):159. doi:10.1186/1471-2164-6-159.
71. Liu Y, Zeng M, Xie Z, Ning D, Zhou J, Yu X, et al. Microbial community structure and ecological networks during simulation of diatom sinking. *Microorganisms*. 2022;10(3):639. doi:10.3390/microorganisms10030639.
72. Rawstern AH, Hernandez DJ, Afkhami ME. Hub taxa are keystone microbes during early succession. *bioRxiv*. 2023; p. 2023.03.02.530218. doi:10.1101/2023.03.02.530218.
73. Yang CH, Jung H. Topological dynamics of the 2015 South Korea MERS-CoV spread-on-contact networks. *Sci Rep*. 2020;10(1). doi:10.1038/s41598-020-61133-9.

74. Paulsson J. Plasmids as stochastic model systems. In: *Fluctuations and Noise in Biological, Biophysical, and Biomedical Systems*. vol. 5110. SPIE; 2003. p. 125–131.
75. Grimm V, Berger U, DeAngelis DL, Polhill JG, Giske J, Railsback SF. The ODD protocol: A review and first update. *Ecol Modell*. 2010;221(23):2760–2768. doi:10.1016/j.ecolmodel.2010.08.019.
76. Harrison E, Jamie Wood A, Dytham C, Pitchford JW, Truman J, Spiers A, et al. Bacteriophages limit the existence conditions for conjugative plasmids. *MBio*. 2015;6(3). doi:10.1128/mBio.00586-15.
77. Neil K, Allard N, Rodrigue S. Molecular mechanisms influencing bacterial conjugation in the intestinal Microbiota. *Front Microbiol*. 2021;12:673260. doi:10.3389/fmicb.2021.673260.
78. Sprouffske K, Wagner A. Growthcurver: an R package for obtaining interpretable metrics from microbial growth curves. *BMC Bioinformatics*. 2016;17(1):172. doi:10.1186/s12859-016-1016-7.
79. Barber MJ. Modularity and community detection in bipartite networks. *Phys Rev E Stat Nonlin Soft Matter Phys*. 2007;76(6 Pt 2):066102. doi:10.1103/PhysRevE.76.066102.
80. Almeida-Neto M, Guimarães P, Guimarães PR Jr, Loyola RD, Ulrich W. A consistent metric for nestedness analysis in ecological systems: reconciling concept and measurement. *Oikos*. 2008;117(8):1227–1239. doi:10.1111/j.0030-1299.2008.16644.x.
81. Newman MEJ, Girvan M. Finding and evaluating community structure in networks. *Phys Rev E Stat Nonlin Soft Matter Phys*. 2004;69(2 Pt 2):026113. doi:10.1103/PhysRevE.69.026113.
82. Estrada E. Quantifying network heterogeneity. *Phys Rev E Stat Nonlin Soft Matter Phys*. 2010;82(6 Pt 2):066102. doi:10.1103/PhysRevE.82.066102.

Supplementary Information: The interplay between ecological networks drives host-plasmid community dynamics

Ying-Jie Wang^{*}, Kaitlin A. Schaal, Johannes Nauta, Armun Liaghat, Manlio De Domenico,
James P. J. Hall, Shai Pilosof^{*}

^{*} Corresponding author: yingjie@post.bgu.ac.il, pilos@bgu.ac.il

This PDF file includes:

S1 Appendix
Figs S1 to S21
Tables S1 to S9

S1 Appendix

Below is the supporting information for the host-plasmid model.

Subpopulation dynamics

The simplified dynamics of plasmid-infected and plasmid-free subpopulations are illustrated in Fig S16. Each subpopulation experiences events that lead to an increase or decrease in abundance at subpopulation-specific per capita rates. Note that for plasmid infection, the infection rate only determines the frequency of infection events, while the rate-independent propensity tensor Γ determines the propensity at which an individual of a given type of plasmid-carrying subpopulation is produced. The equations and related parameters of the per capita rates and the propensity tensor are described in Materials and Methods.

Input and output

The raw simulation input is in JSON format and includes the variables described in Table Table S6. The raw simulation output is in SQLite format and includes three tables. Table "bsubabundance" is the table of host subpopulation dynamics. It includes time (**t**), subpopulation id (**subpop_id**), host id, plasmid profile (**p_profile**), and subpopulation abundances (**abundance**). Table "events" includes time (**t**), the accumulated number of growth events (**growth**), death events (**death**), segregation events (**segregation**), competition events (**competition**), and infection events (**infection**). Table "meta" includes the general information about the simulation: **seed**, **key** (the id of a simulation and output assigned by the experiment designer), **job** (the id of the job generated by the HPC), **start time**, **end time**, and **elapsed seconds**.

Results from an alternative model with density-dependent growth

To explore how density-dependent growth (a typical competitive Lotka-Volterra model) affect the results, we re-defined the subpopulation per capita growth rate as

$$\eta_{i,p} = \eta_i \left(1 - \frac{H_i}{K}\right) \prod_{\alpha|p_\alpha \neq 0} (1 - c_\alpha), \quad (1)$$

and removed the competition event. The results were qualitatively identical and quantitatively strengthened: a structured plasmid compatibility network **P** promotes transient host coexistence (Fig S17), while a modular infection network **I** promotes stable host coexistence and plasmid diversity (Figs S18 and S19). Also, network structure can counteract the effects of one another. For example, the hub plasmid P1 at hub **P** failed to be prevalent at modular **I** (Figs S19 and S20). The strengthened patterns were due to the density-dependent growth (indirect competition), which limits population growth more efficiently (without time delay) than direct competition events in a stochastic model. Such indirect rather than direct competition delayed competitive exclusion and thereby enhanced host coexistence.

Complexity-dependent computational efficiency

To demonstrate how the system complexity limits the computational efficiency of our model, we ran a model performance test across n-host-n-plasmid systems where n ranged from one to six. Each n-host-n-plasmid system was initialized with $n \times (n + 1)$ subpopulations, where each host population had a plasmid-free subpopulation with 1000 individuals, and all potential single-plasmid-carrying subpopulations with 100 individuals each. We fixed all the host and plasmid traits across populations, applied the reference (full) structure for all interaction networks, and increased the community-wide carrying capacity K linearly with the initial number of subpopulations (Table Table S7). The elapsed time for the infection tensor Γ generation, initialization and simulation substantially increased with system complexity (Fig S21).

Figs S1 to S21

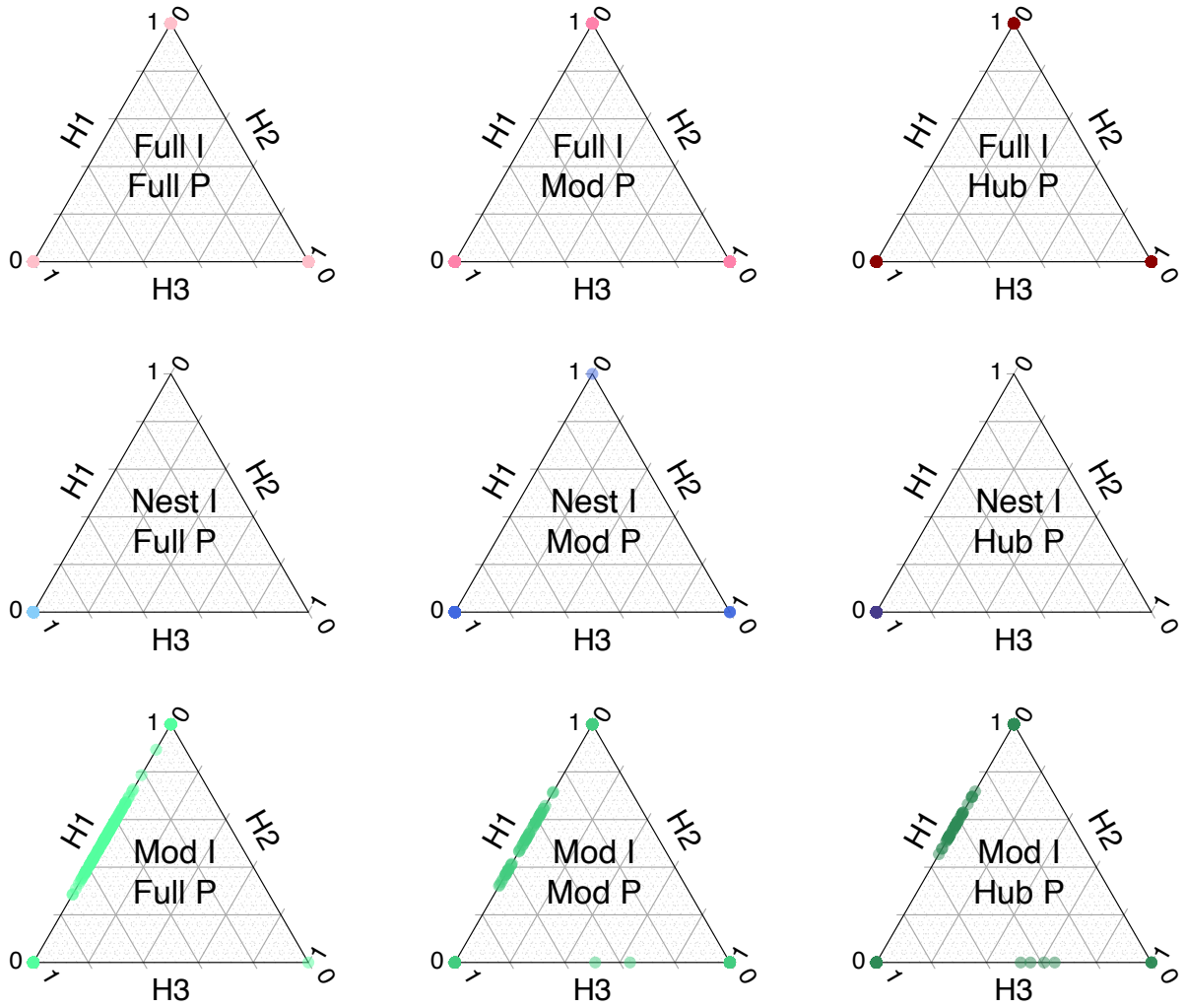


Fig S1. Relative abundance of populations at the end of the simulations ($t = 20000$ hours). Dots on the vertices represent no coexistence (i.e. only one population survived), while dots on the edges represent the coexistence of two populations.

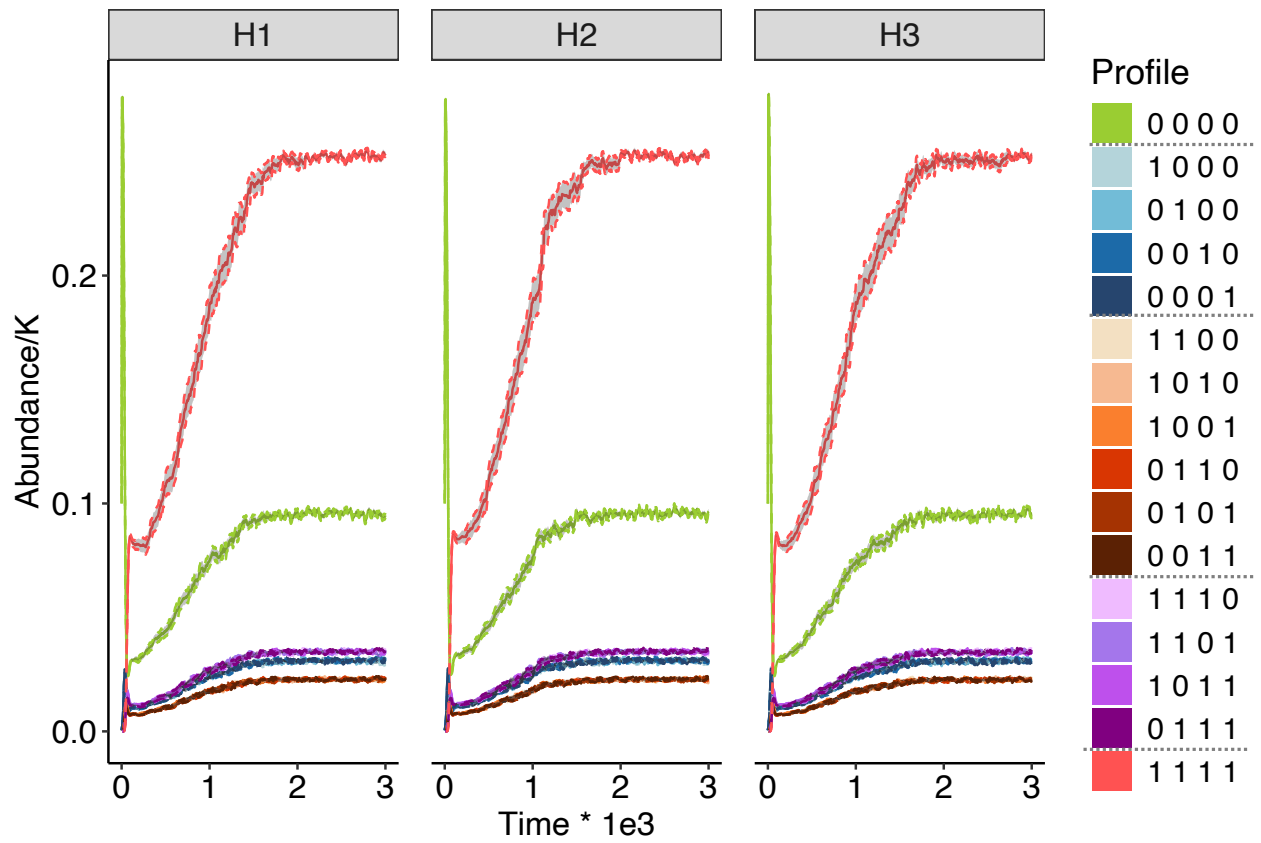


Fig S2. Dynamics of subpopulation abundance (mean \pm 1 SE) at full I x full P. Note that the number of replicates of a subpopulation at a given time point may vary across time, for it depends on how many replicates still have that subpopulation at that time point. The K at y-axis represents carrying capacity. Time was only plotted to $t = 3000$ where equilibrium of subpopulations had been reached. Note the plasmid-free subpopulation (green line) first increased then decreased.

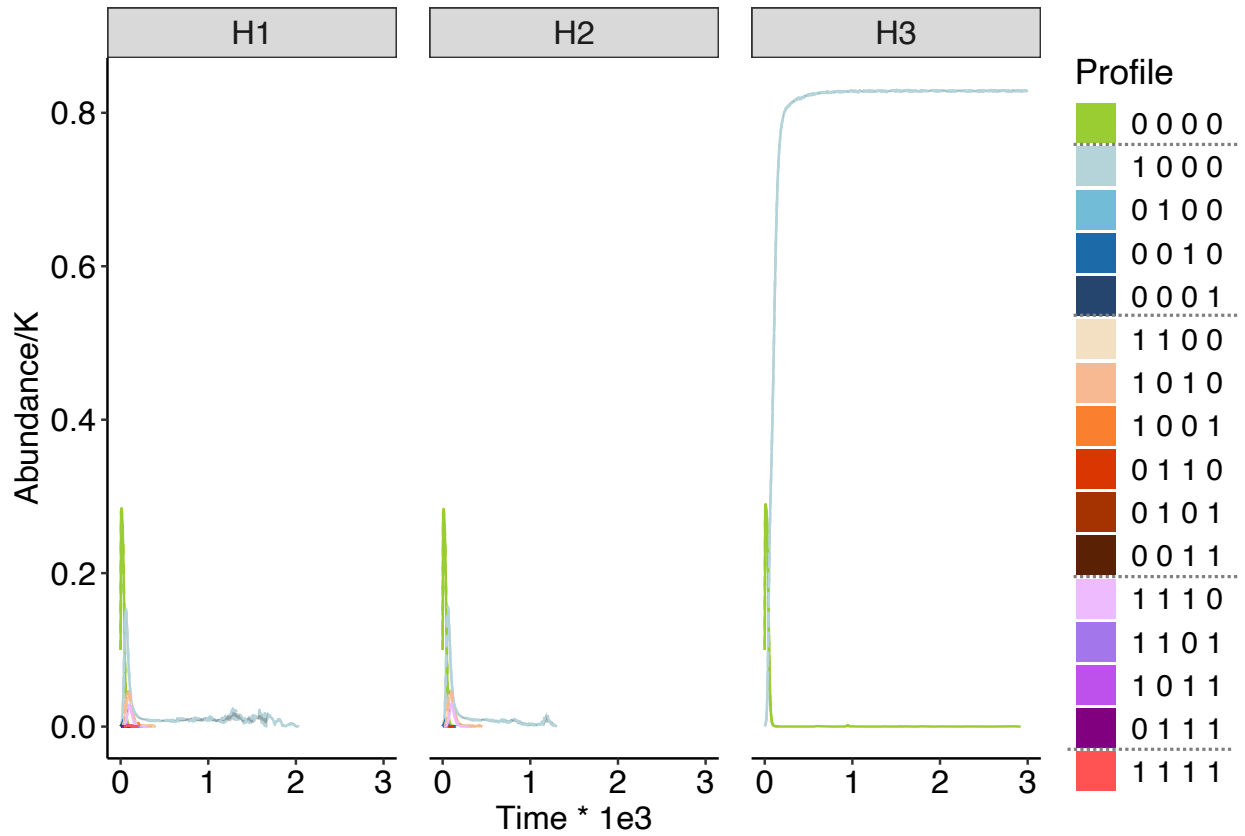


Fig S3. Dynamics of subpopulation abundance (mean \pm 1 SE) at nested I x full P. Note that the number of replicates of a subpopulation at a given time point may vary across time, for it depends on how many replicates still have that subpopulation at that time point. The K at y-axis represents carrying capacity. Time was only plotted to $t = 3000$ where equilibrium of subpopulations had been reached.

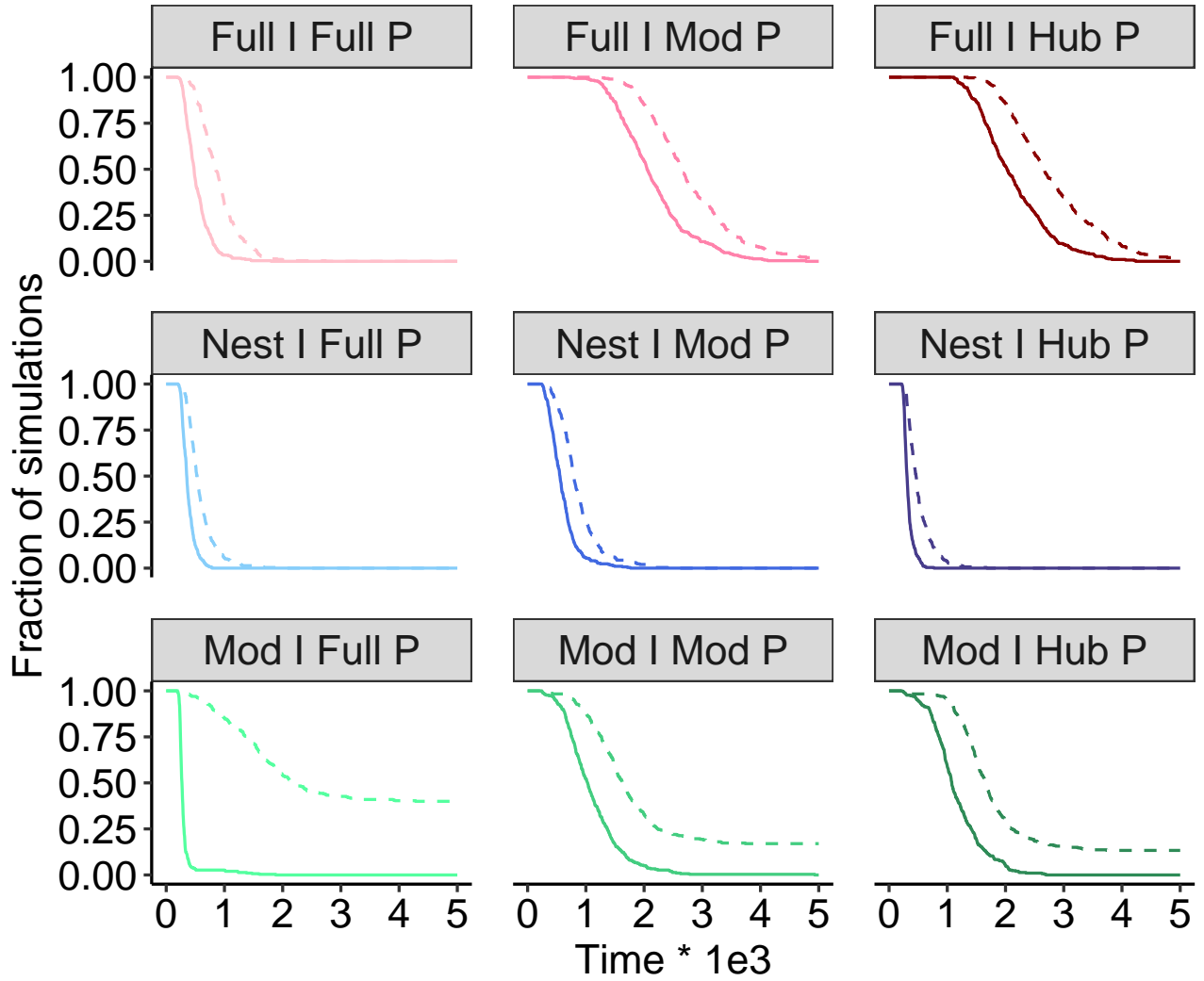


Fig S4. Dynamics of microbe coexistence of three populations (solid line) and two populations (dashed line) at the end of the simulations ($t = 20000$ hours). The dynamics of microbe coexistence probability (fraction of simulations) is calculated as the proportion of replicates with complete(3-population)/partial(2-population) coexistence out of total number of replicates across time. Time was only plotted to $t = 5000$ where all probabilities had dropped to zero.

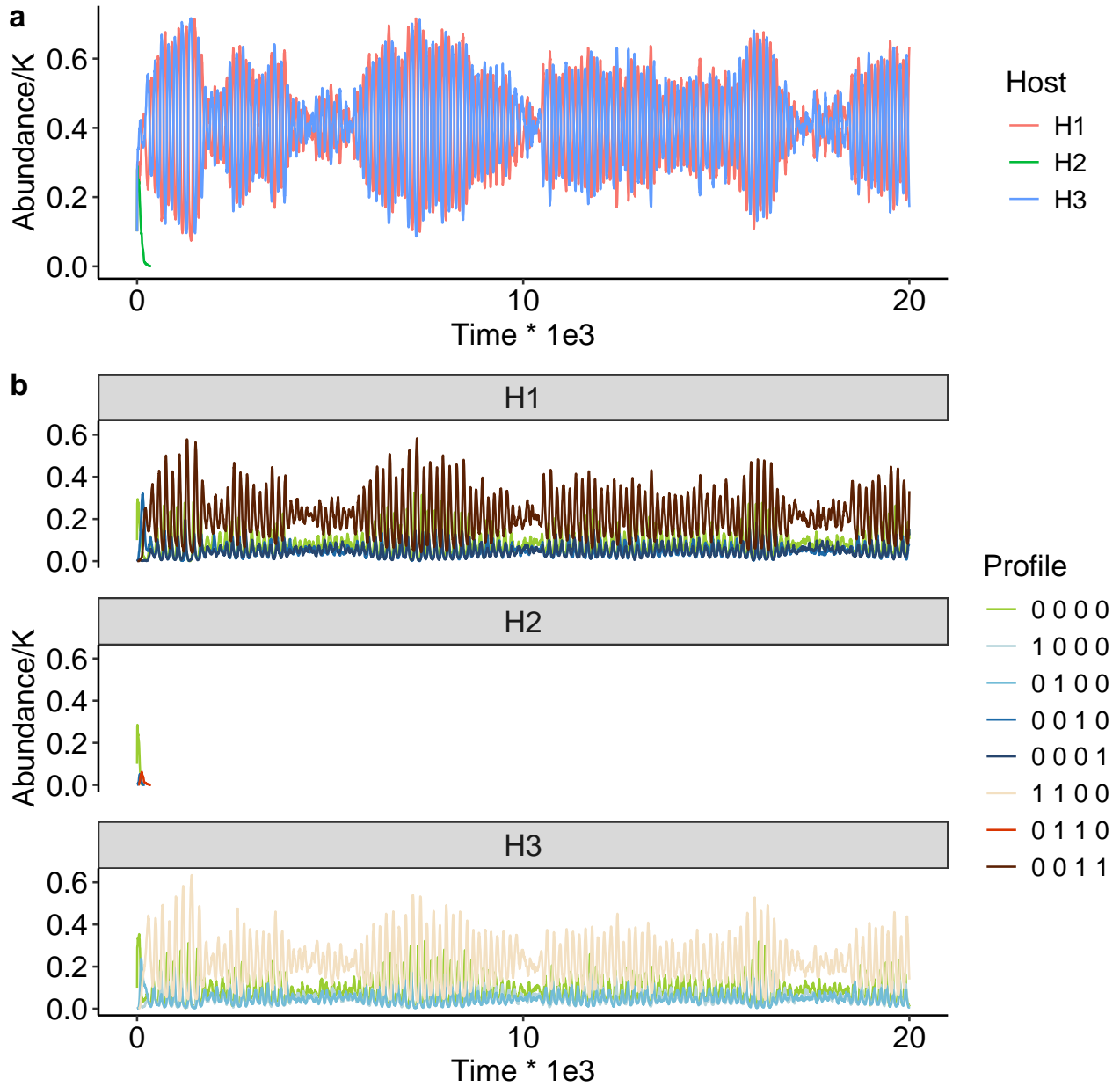


Fig S5. Dynamics of (a) population abundance and (b) subpopulation abundance at modular I x full P from replicate 21. Replicate 21 demonstrated the stable coexistence scenario where the plasmid-free subpopulations of the peripheral hosts persisted. The K at y-axis represents carrying capacity. Interestingly, populations and subpopulations fluctuated with alternative amplitudes around mean abundance. This is because there was a dynamical balance between primary and secondary plasmid infections between the coexisting hosts.

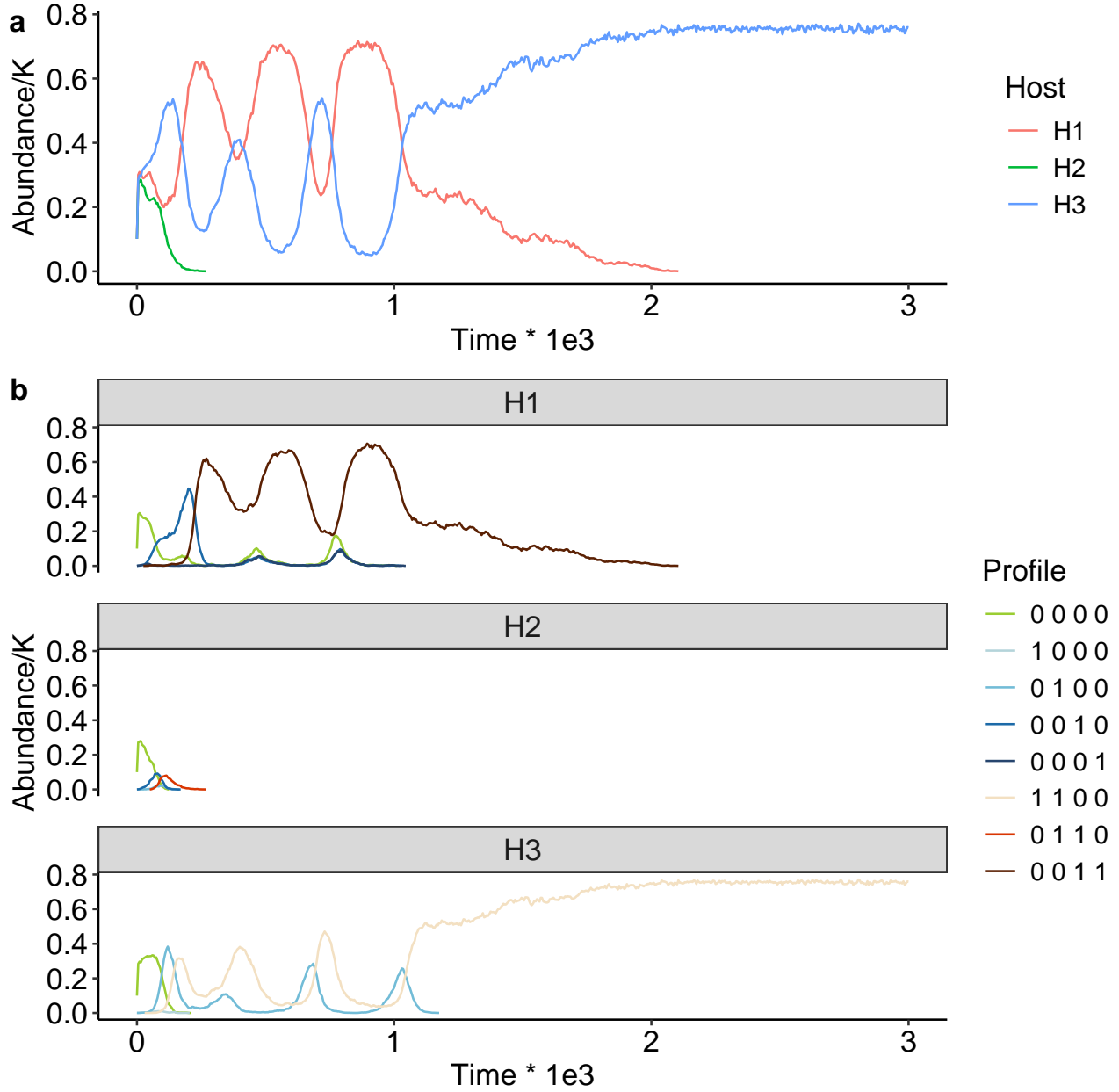


Fig S6. Dynamics of (a) population abundance and (b) subpopulation abundance at modular I x full P from replicate 23. Replicate 23 demonstrated the unstable coexistence scenario where the plasmid-free subpopulations of the peripheral hosts went extinct. When the plasmid-free subpopulations went extinct, monoplasmidic subpopulations lost input from infection, and the remaining monoplasmidic individuals quickly got co-infected, destabilizing the oscillatory dynamics of the coexisting populations. The K at y-axis represents carrying capacity. Time was only plotted to $t = 3000$ where equilibrium of subpopulations had been reached.

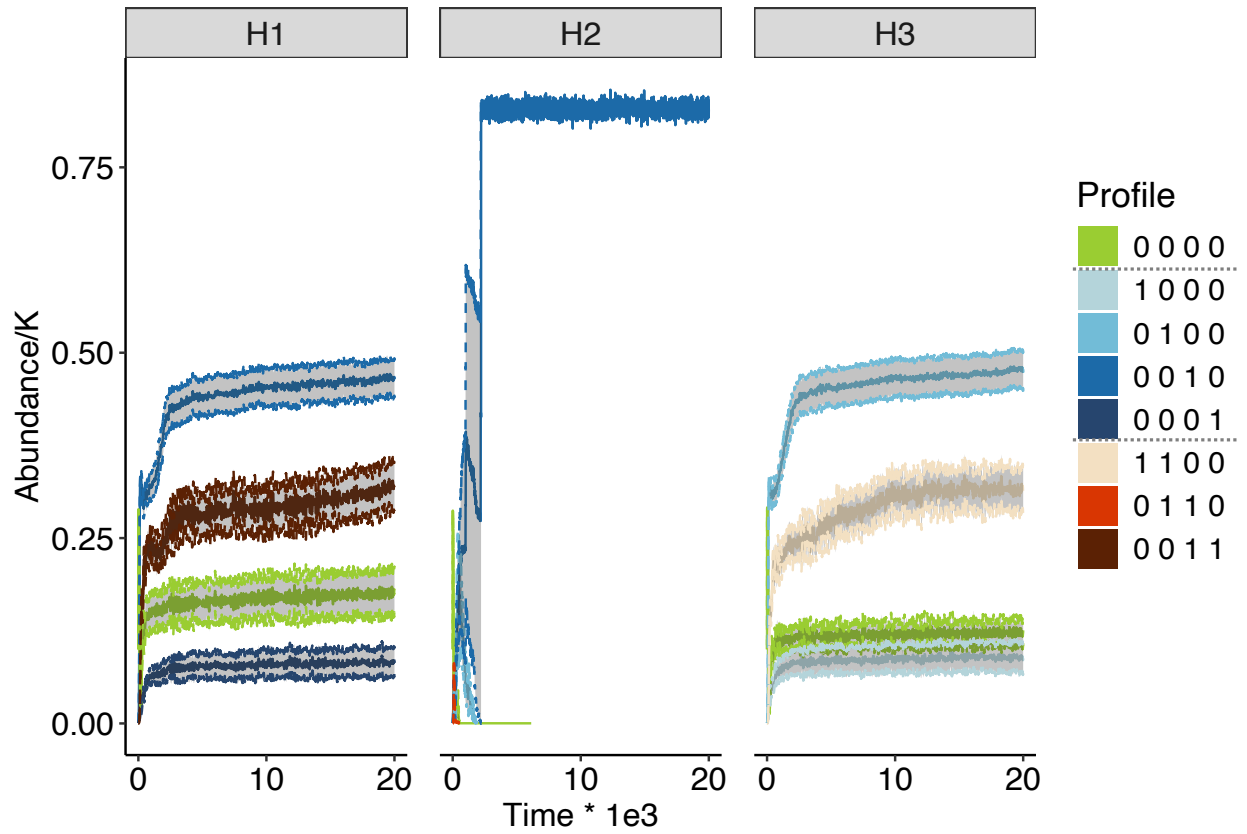


Fig S7. Dynamics of subpopulation abundance (mean \pm 1 SE) at modular I x full P. Note that the number of replicates of a subpopulation at a given time point may vary across time, as it depends on how many replicates still have that subpopulation at that time point. The K at y-axis represents carrying capacity. The high abundance of P3-infected H2 is from a rare case (one from 300 replicates).

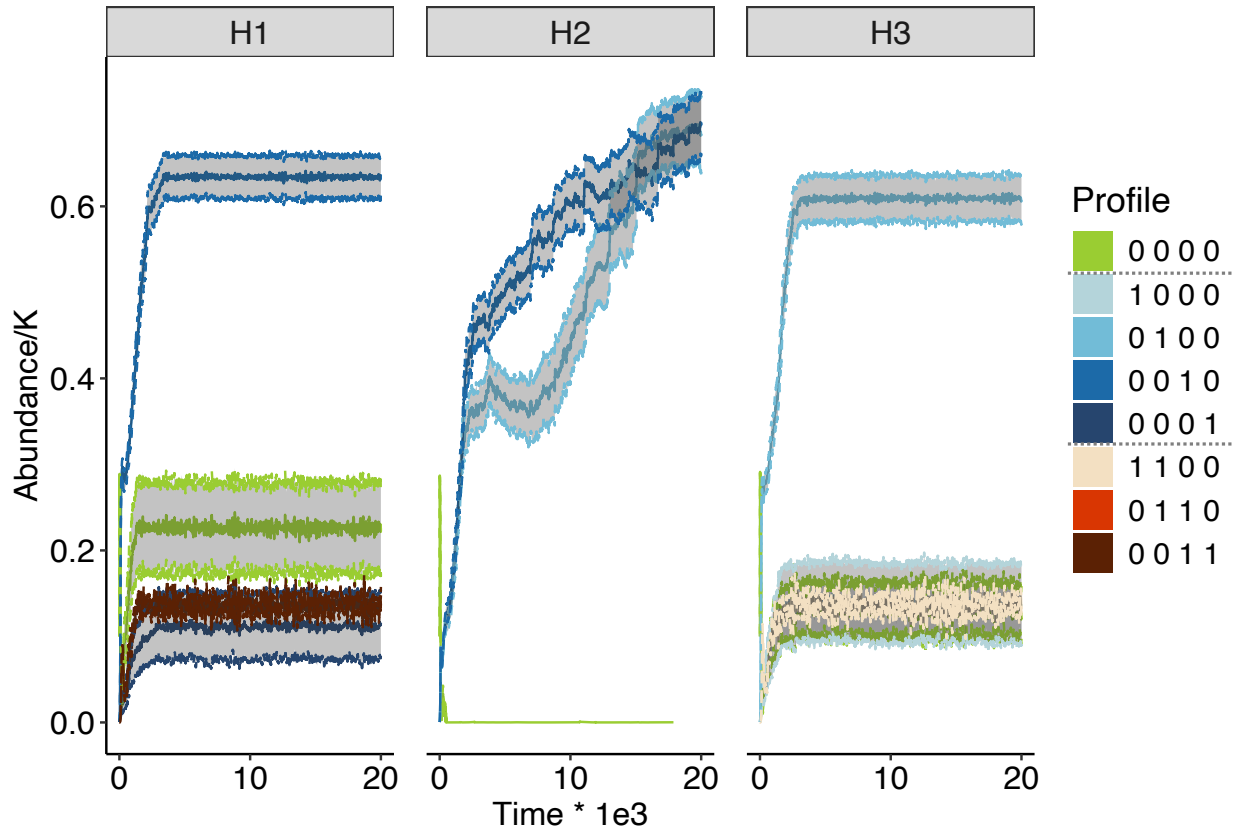


Fig S8. Dynamics of subpopulation abundance (mean \pm 1 SE) at modular I x modular P. Note that the number of replicates of a subpopulation at a given time point may vary across time, for it depends on how many replicates still have that subpopulation at that time point. The K at y-axis represents carrying capacity. The subpopulation abundances of H2 are from 65 replicates.

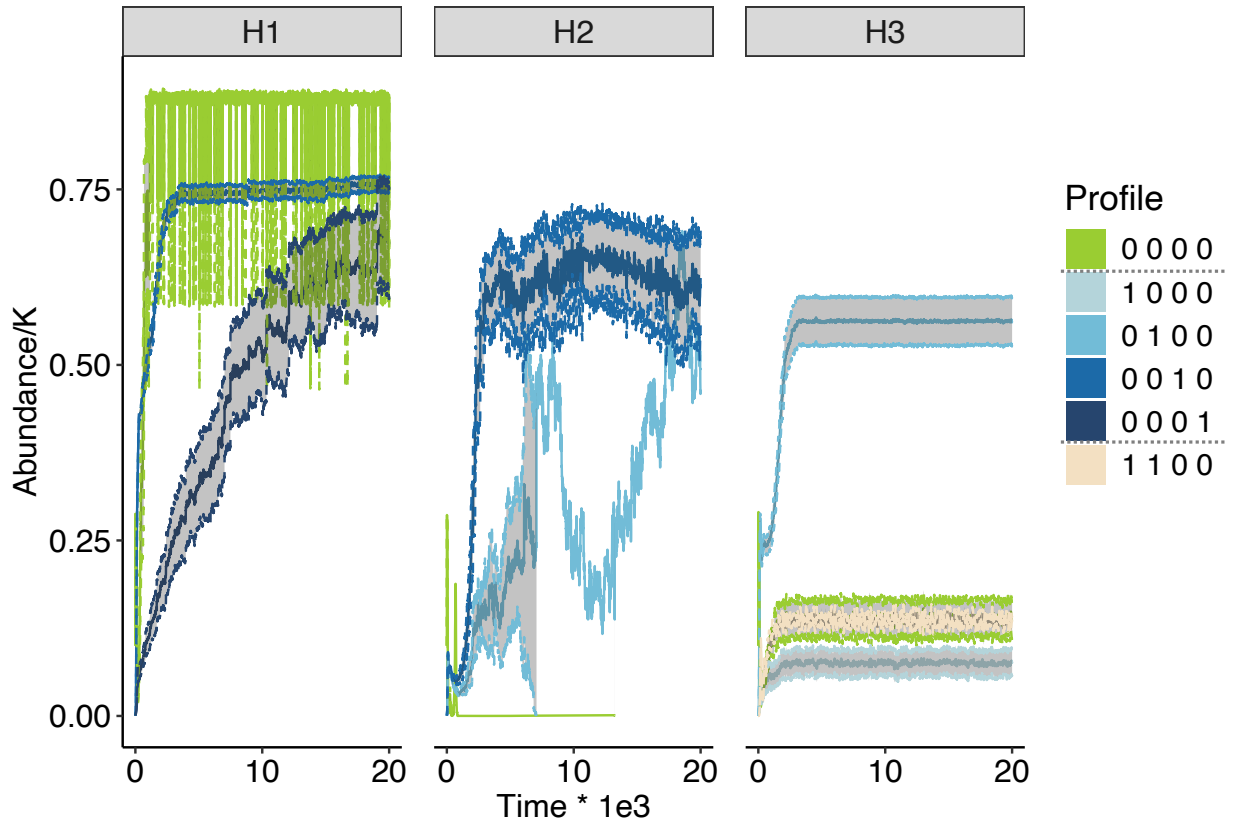


Fig S9. Dynamics of subpopulation abundance (mean \pm 1 SE) at modular I x hub P. Note that the number of replicates of a subpopulation at a given time point may vary across time, for it depends on how many replicates still have that subpopulation at that time point. The K at y-axis represents carrying capacity. The subpopulation abundances of H2 are from 9 replicates.

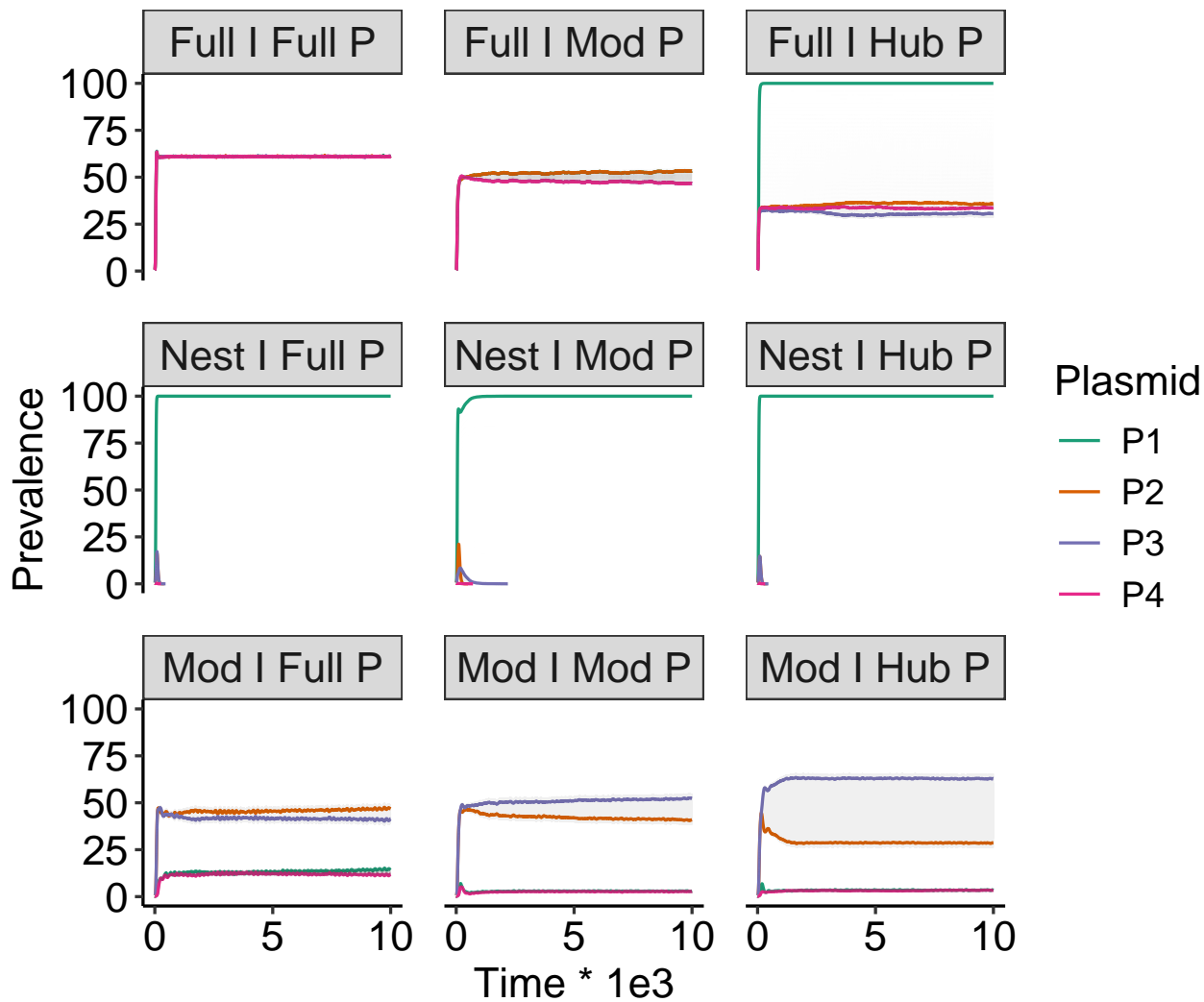


Fig S10. Dynamics of plasmid prevalence (mean \pm 1 SE). Time was only plotted to $t = 10000$ where equilibrium of plasmid prevalence had been reached.

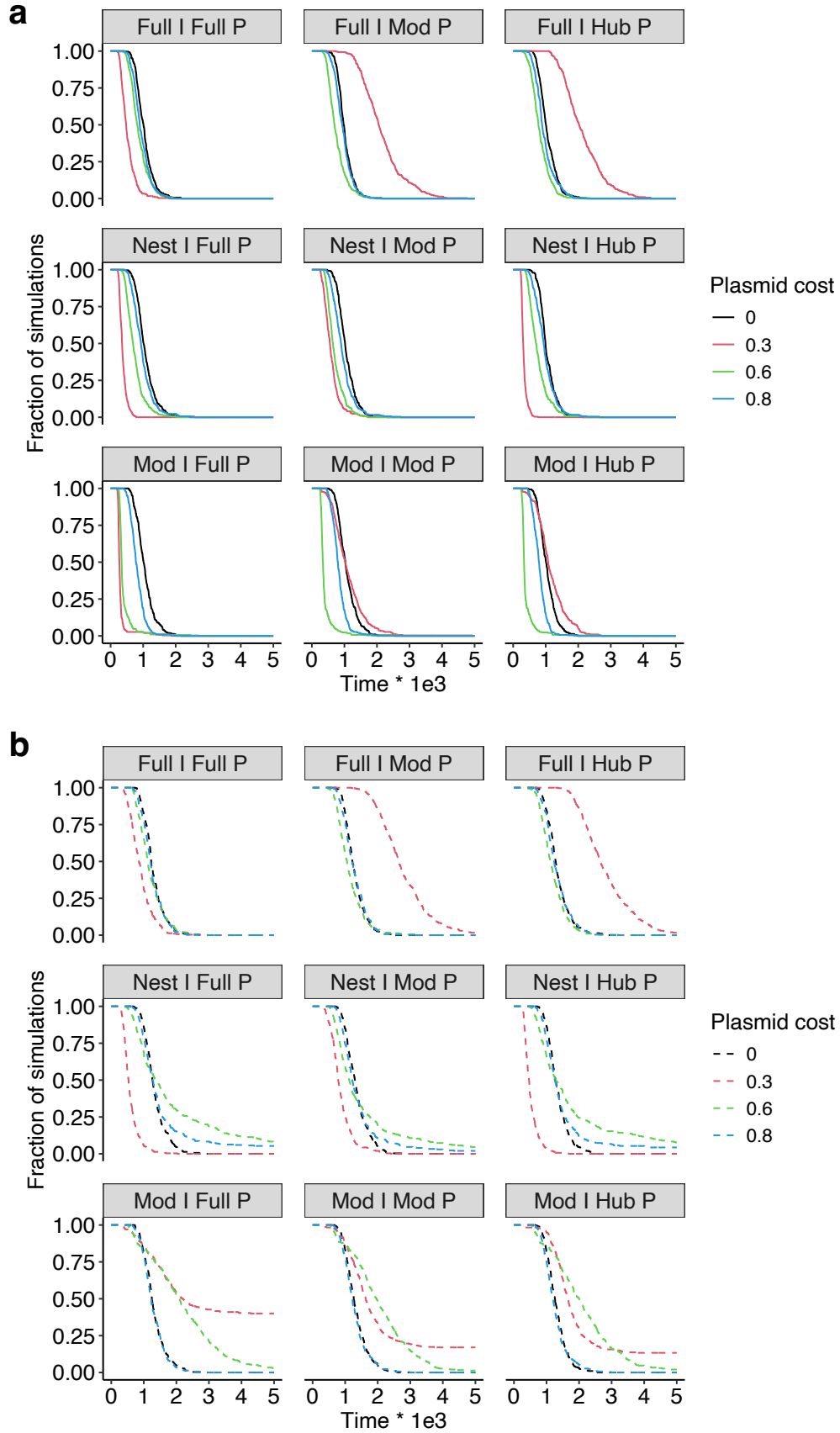


Fig S11. Dynamics of microbe coexistence of (a) three populations (solid line) and (b) two populations (dashed line) across plasmid costs. The dynamics of coexistence probability (fraction of simulations) is calculated as the proportion of replicates with complete(3-population)/partial(2-population) coexistence out of total number of replicates across time. Time was only plotted to $t = 5000$ where most probabilities had dropped to zero.

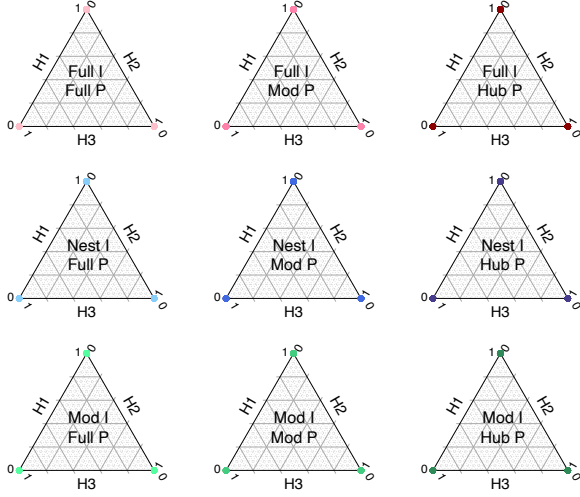
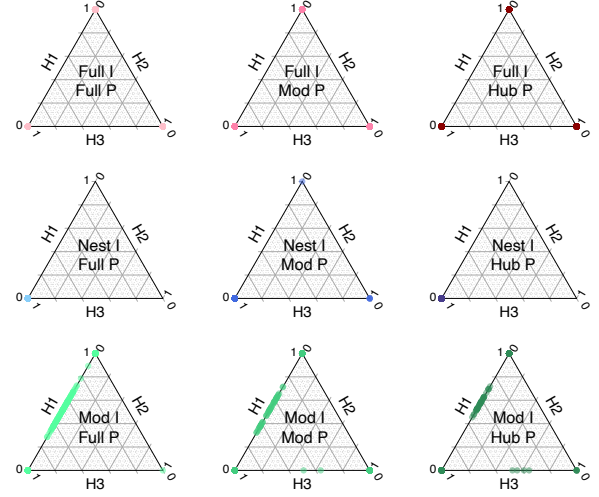
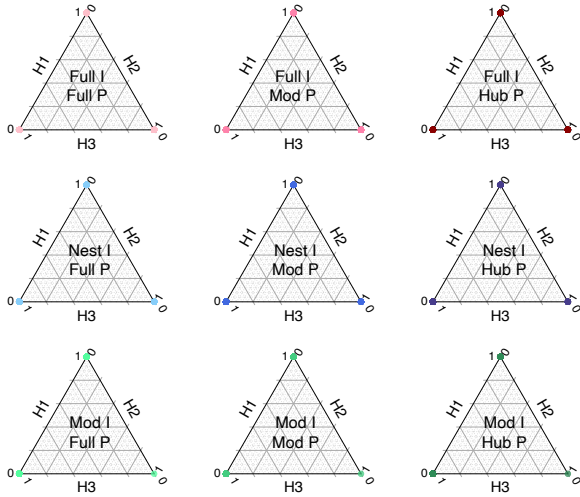
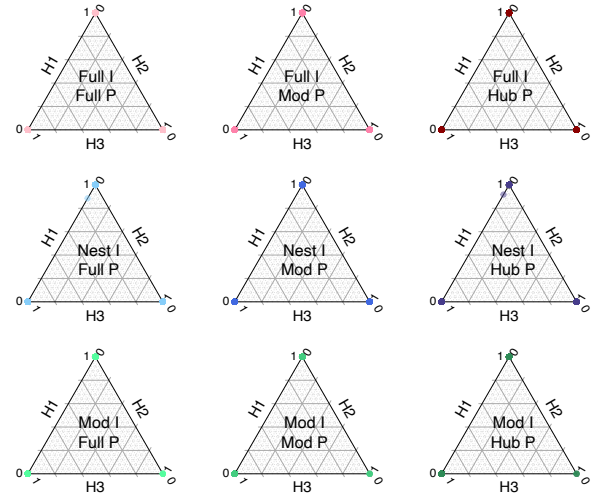
a Plasmid cost = 0**b** Plasmid cost = 0.3**c** Plasmid cost = 0.6**d** Plasmid cost = 0.8

Fig S12. Relative abundance of populations at the end of the simulations ($t = 20000$ hours) when plasmid cost = (a) 0, (b) 0.3, (c) 0.6, and (d) 0.8. Dots on the vertices represent no coexistence (i.e. only one population survived), while dots on the edges represent the coexistence of two populations.

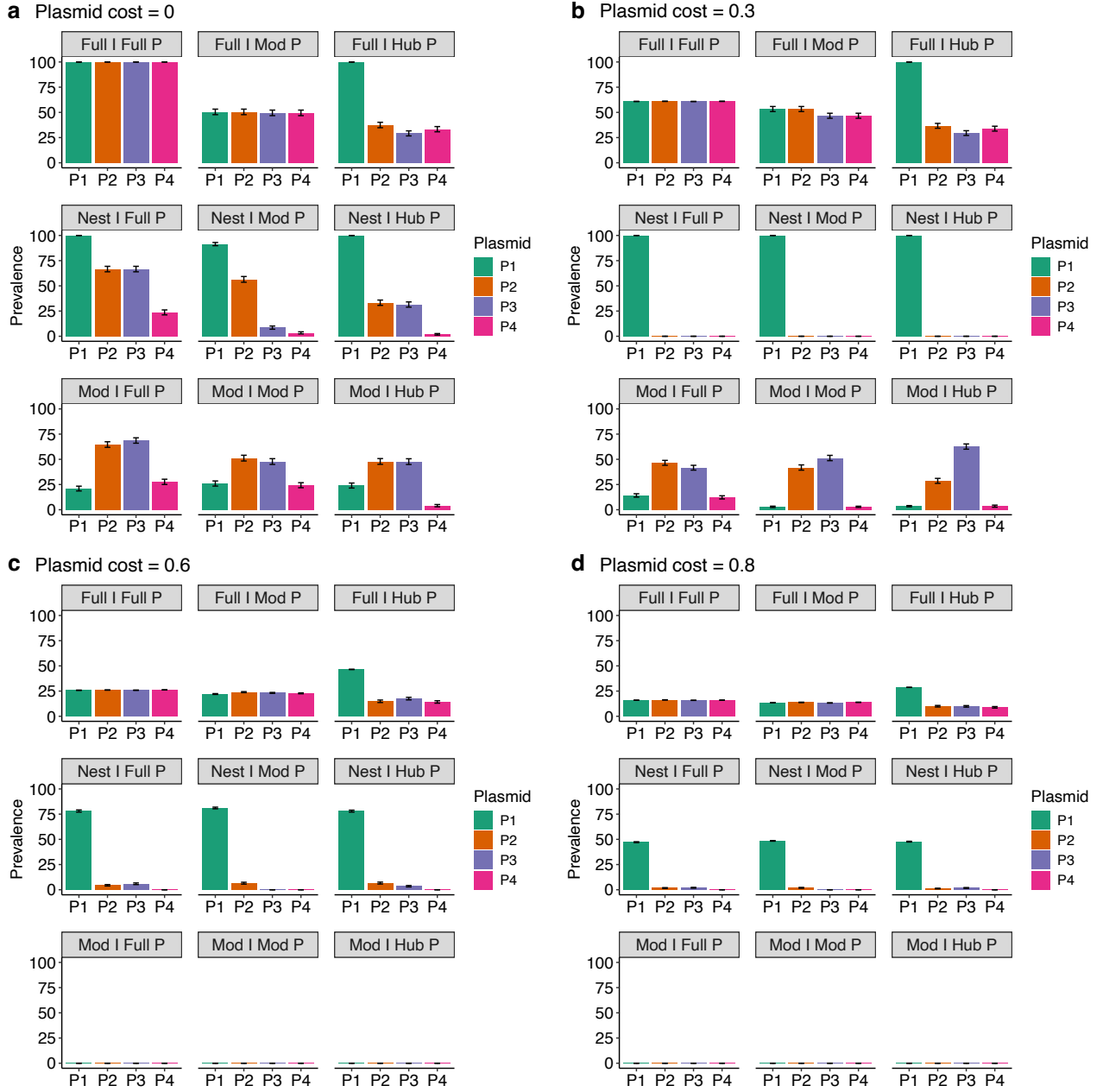


Fig S13. Mean and SE of final plasmid prevalence across all replicates when plasmid cost = (a) 0, (b) 0.3, (c) 0.6, and (d) 0.8.

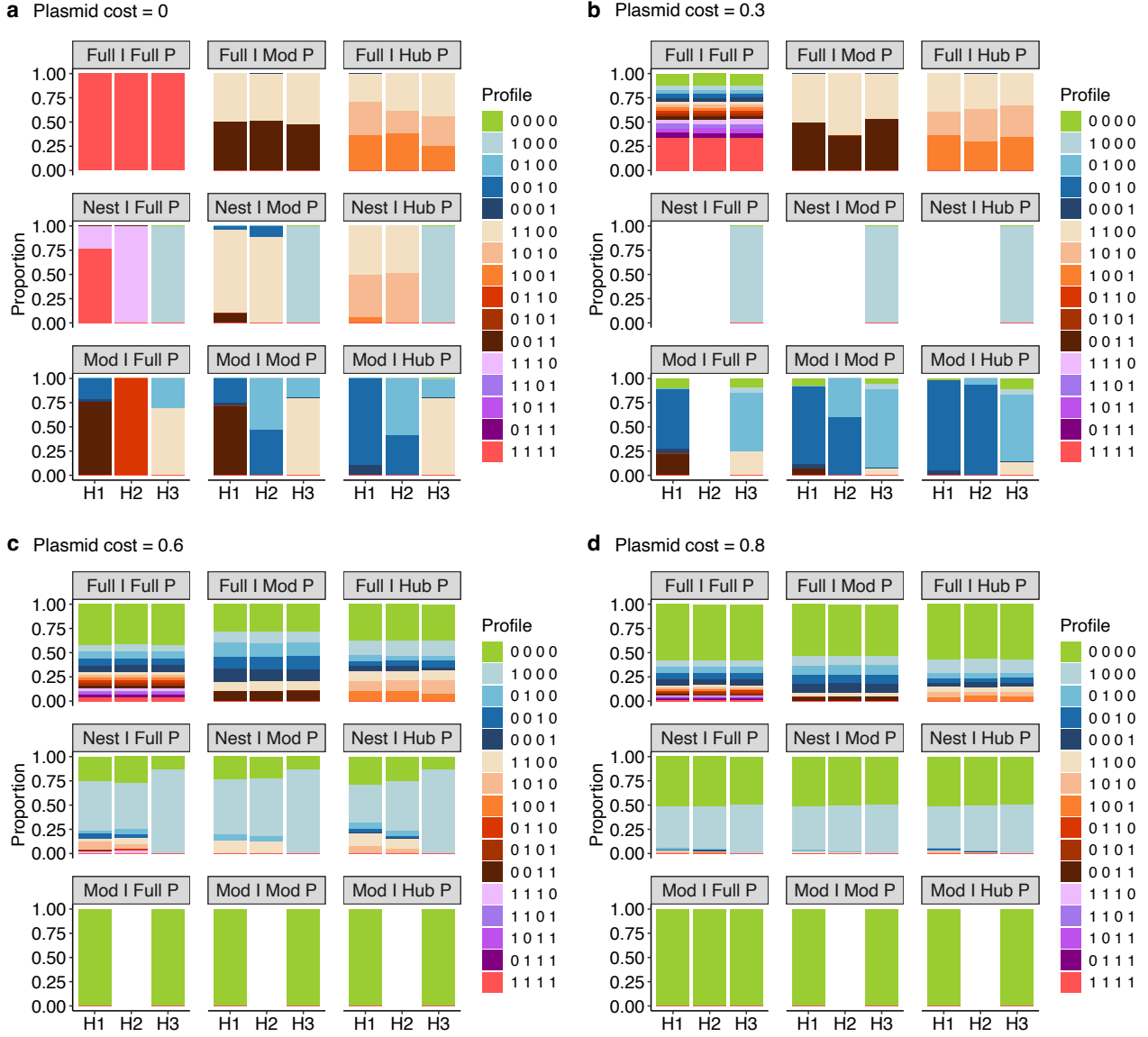


Fig S14. Final host population composition when plasmid cost = (a) 0, (b) 0.3, (c) 0.6, and (d) 0.8., averaged across replicates in which that host population survived (only populations surviving in > 5 replicates were considered). Profiles represent the host subpopulations (e.g., the profile 1000 represents a subpopulation hosting only P1).

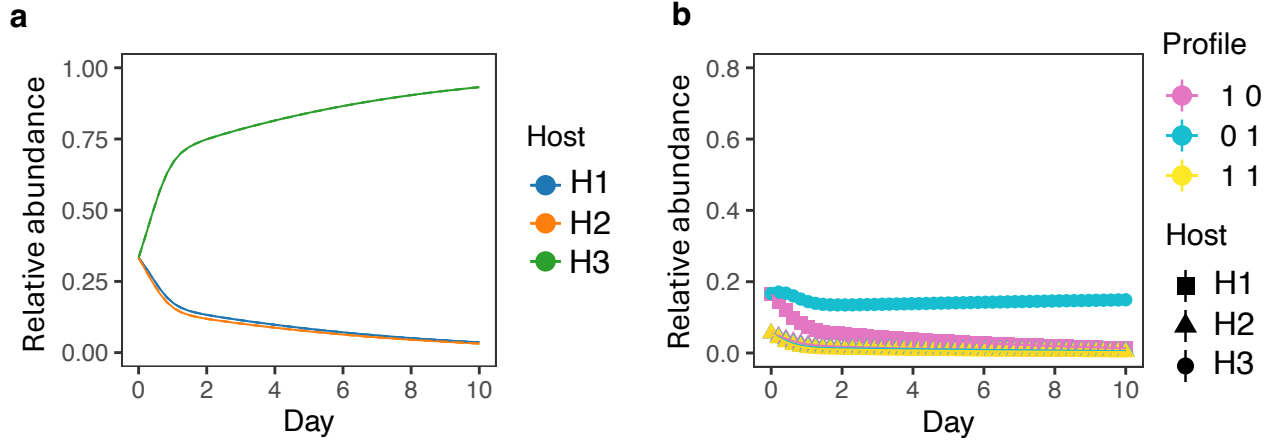


Fig S15. (a) The host population dynamics and (b) host subpopulation dynamics from the simulations assuming no increase on the growth rate of the bridge host H2 under a modular **I** based on an empirical system (Figure 5a, top row).

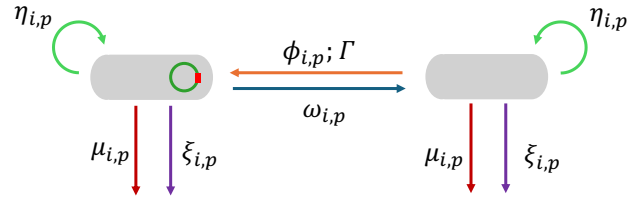


Fig S16. Illustration of the dynamics of plasmid-carrying subpopulation (left box with a circle in it) and plasmid-free subpopulation (right box). Colored arrows indicate abundance inflows/outflows from the five events: growth (green), death (red), competition (purple), infection (orange), and segregation (blue). Alongside each arrow lists the per capita rate of the event, with subscripts denoting host i and plasmid profile p of the subpopulation.

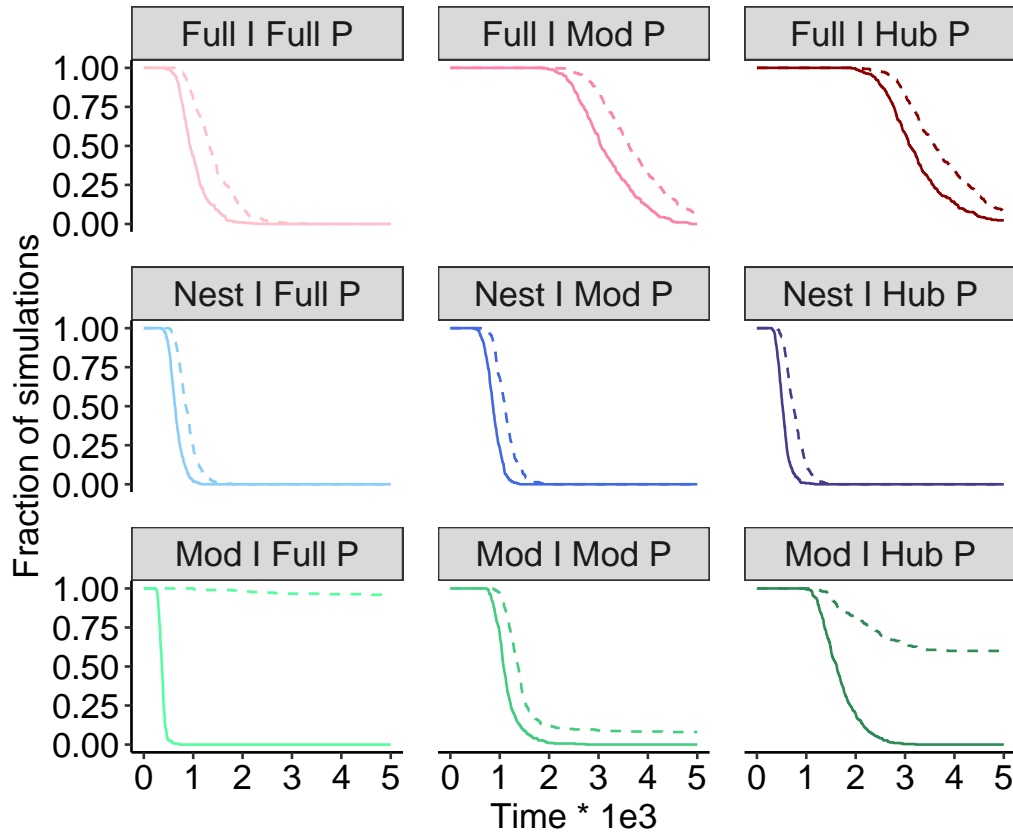


Fig S17. Dynamics of microbe coexistence of three populations (solid line) and two populations (dashed line) under density-dependent growth. The dynamics of coexistence probability (fraction of simulations) is calculated as the proportion of replicates with complete(3-population)/partial(2-population) coexistence out of total number of replicates across time. Time was only plotted to $t = 5000$ where most probabilities had dropped to zero or stabilized.

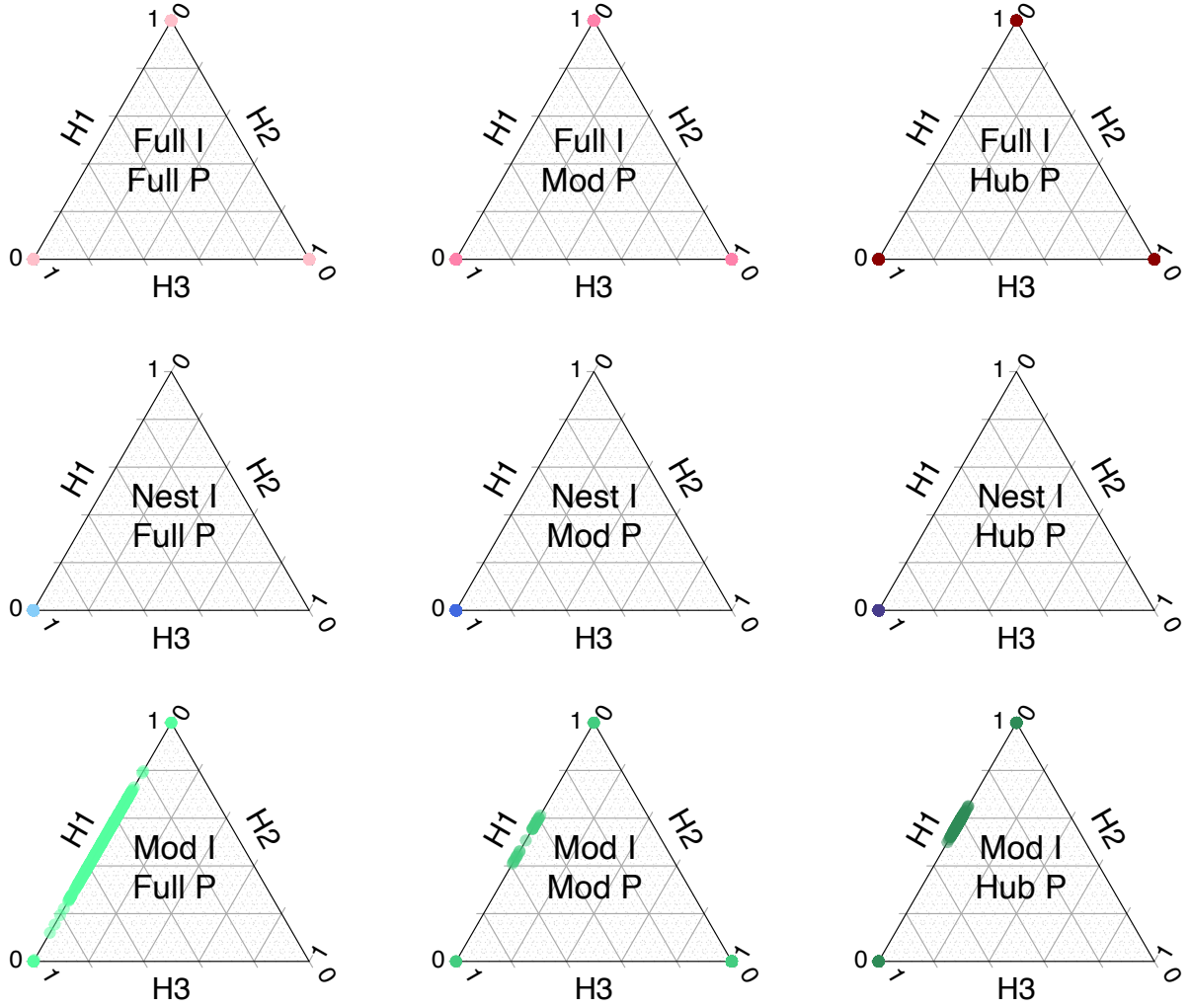


Fig S18. Relative abundance of populations at the end of the simulations ($t = 20000$ hours) under density-dependent growth. Dots on the vertices represent no coexistence (i.e. only one population survived), while dots on the edges represent the coexistence of two populations.

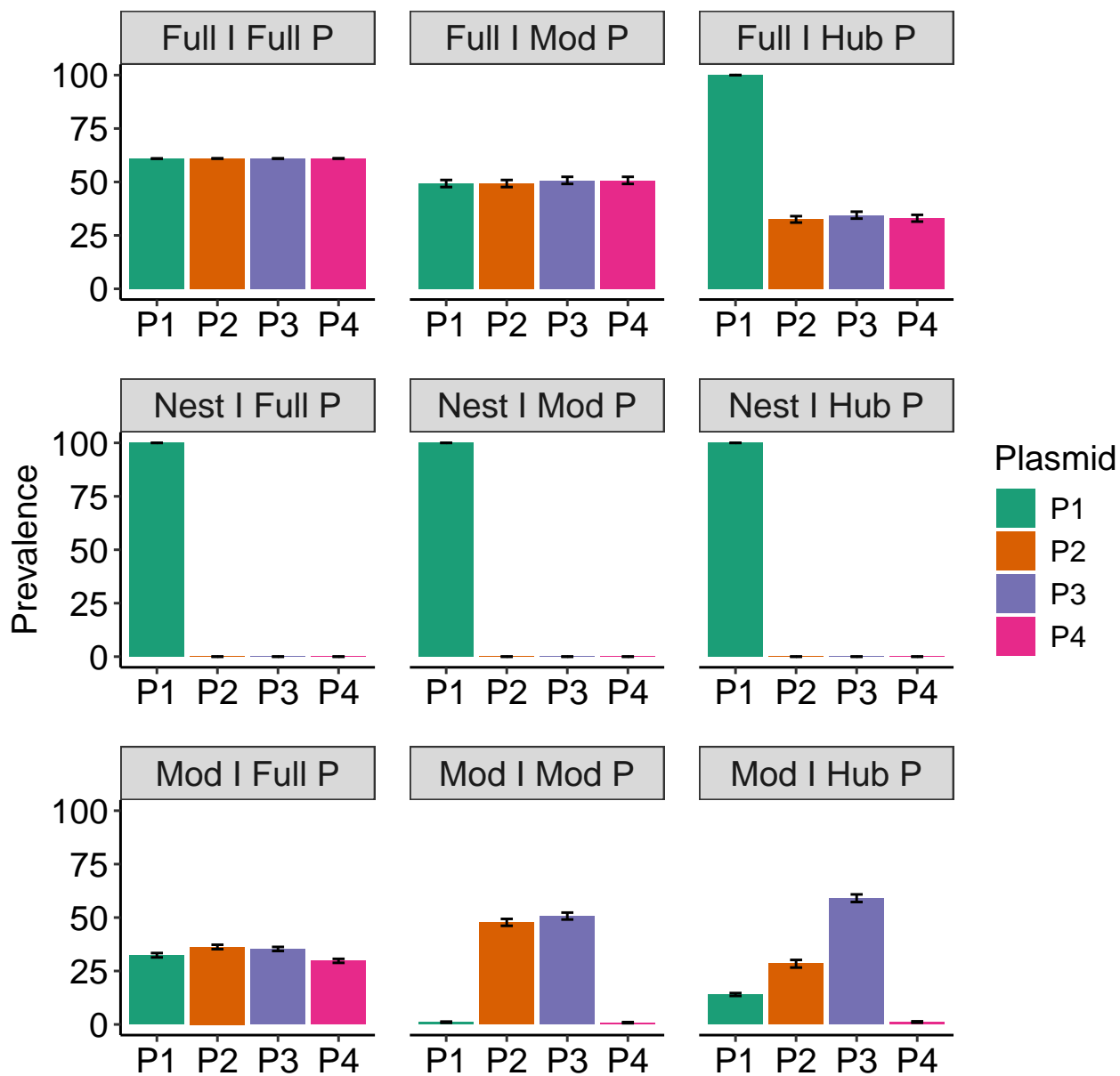


Fig S19. Mean and SE of final plasmid prevalence across all replicates under density-dependent growth.

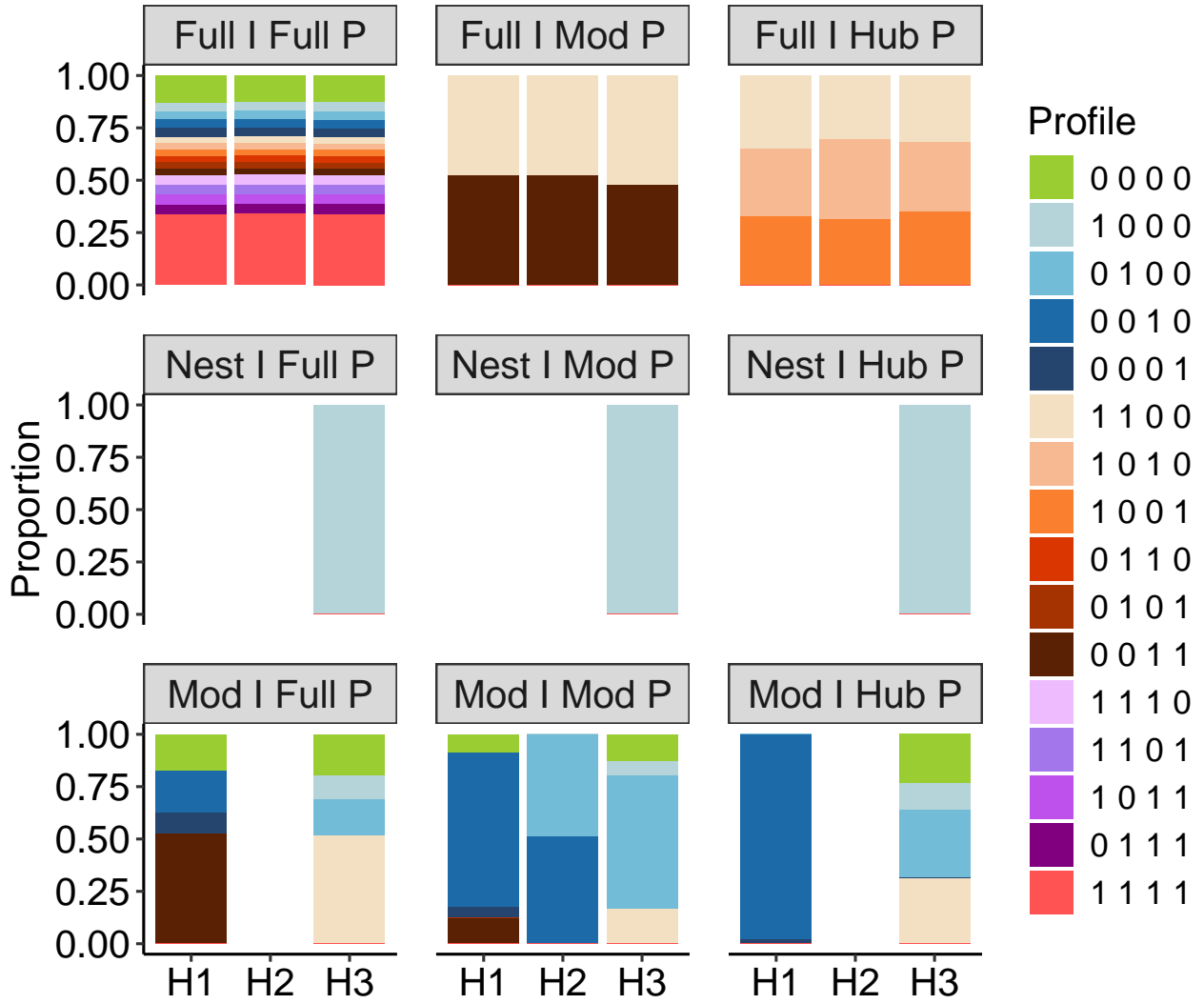


Fig S20. Final host population composition under density-dependent growth, averaged across replicates in which that host population survived (only populations surviving in > 5 replicates were considered). Profiles represent the host subpopulations (e.g., the profile 1000 represents a subpopulation hosting only P1).

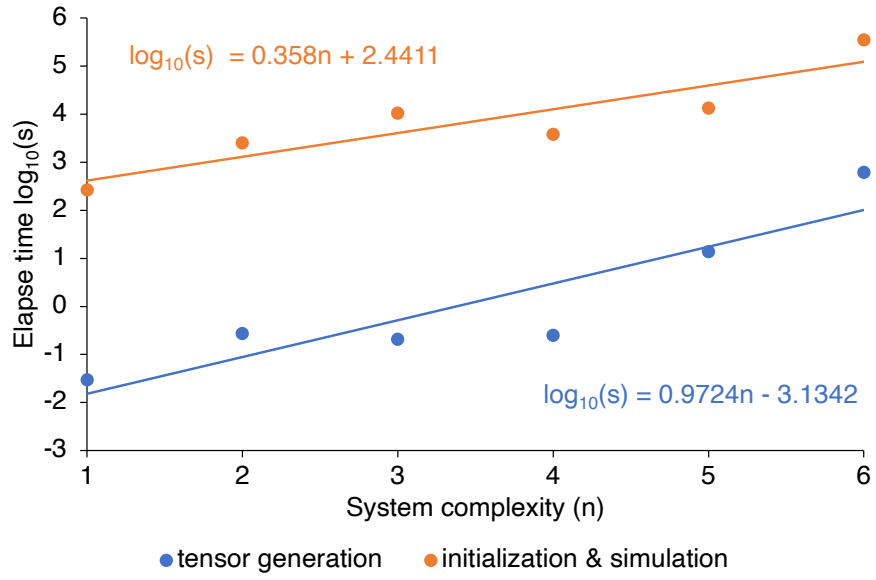


Fig S21. Elapse time of tensor generation, initialization and simulation across system complexity n , i.e. the number of host and plasmid populations in the system.

Tables S1 to S7

Table S1. Host-specific parameters. The net population growth rates were parameterized using the empirical data fit to the standard form of the logistic equation in the R package *growthcurver* [1], while the population growth rates and death rates were arbitrarily assigned to match the net population growth rate. The infection rates and competition coefficients were assigned in a relative magnitude in order to better match the empirical subpopulation and population dynamics. The segregation rates were fixed to an extremely low value so these can be negligible. The community-wise carrying capacity was arbitrarily assigned for computational efficiency. We later assumed an increase in the growth rate of the bridge host (H2).

Host traits	H1	H2	H3
growth rate η_i	0.1	0.15*	0.2
death rate μ_i	0.01	0.01	0.01
infection rate $\phi_{i,p}$	5e-9	5e-9	5e-8
segregation rate e_i	1e-8	1e-8	1e-8
competition coefficient on H1 a_{1i}	1	0.02	0.03
competition coefficient on H2 a_{2i}	5e-3	1	0.03
competition coefficient on H3 a_{3i}	5e-3	0.02	1
perturbation impact ϵ_i	0	0.0	0.0
community-wise carrying capacity K	1e5	1e5	1e5

* Set to 0.1 under the assumption of no increase in the growth rate of H2.

Table S2. Plasmid-specific parameters. The plasmid costs were assigned in a relative magnitude based on empirical monocultures of the infected bridge host population in order to better match the empirical subpopulation and population dynamics. The plasmid resistance to stress was arbitrarily assigned and fixed as these are irrelevant for systems without stress.

Plasmid traits	P1	P2
plasmid cost c_α	0.2	0.4
plasmid resistance ρ_α	0.7	0.7

Table S3. Initial abundance of the plasmid-present system for a modular infection network **I**.

Host i	Plasmid profile p	Abundance $H_{i,p}$
1	[0,0]	1650
1	[1,0]	1650
2	[0,0]	1650
2	[1,0]	550
2	[0,1]	550
2	[1,1]	550
3	[0,0]	1650
3	[0,1]	1650

Table S4. Initial abundance of the plasmid-present system for a full infection network **I**.

Host i	Plasmid profile p	Abundance $H_{i,p}$
1	[0,0]	1650
1	[1,0]	550
1	[0,1]	550
1	[1,1]	550
2	[0,0]	1650
2	[1,0]	550
2	[0,1]	550
2	[1,1]	550
3	[0,0]	1650
3	[1,0]	550
3	[0,1]	550
3	[1,1]	550

Table S5. Constants and parameters for the model.

Variable	Definition	Type
t	time	float
t_{final}	time scale of the simulation	float (h)
n_b	number of host populations in the system	integer
n_p	number of plasmids in the system	integer
i, j, k	host of the entity	integer
p, q, r	plasmid profile of the entity	integer
α	plasmid α	integer
$H_{i,p}$	entity and abundance of a host subpopulation	integer
H_i	abundance of host i	integer
K	community-wise carrying capacity of host	float
e_i	probability of segregation error of host i	float
μ_i	per capita death rate of host i	float
η_i	per capita growth rate of host i	float
$\phi_{i,p}$	per capita infection rate of host subpopulation $H_{i,p}$	float
$\gamma_{i,p}$	infection coefficient of host subpopulation $H_{i,p}$	float
ρ_α	resistance of plasmid α	float
c_α	cost of plasmid α on host growth	float
A	host competition matrix	matrix of floats
H	HGT matrix	matrix of floats
I	infection matrix	matrix of integers
P	plasmid compatibility matrix	matrix of integers
Γ	propensity tensor of infection	3-D tensor of floats

Table S6. Variables for the model input.

Condition	Content	Type (v(): vector of ())
t_final	t at which simulation ends	float
t_output	the t interval after which state is recorded	float
rng_seed	seed for the simulation	null;float
n_seeds	the number of seed for the simulation	integer; 1
n_bstrains	n_b maximum number of host populations in the system	integer
n_pstrains	n_p maximum number of plasmids in the system	integer
n_bsubstrains	number of subpopulations at initial state	integer
strain_id_for_each_substrain	host id i of subpopulations	integer
n_ind_bsubstrains	abundance of subpopulations	integer
p_profile_bsubstrains	the plasmid profile p of subpopulations	v(v(s) of binary element(s))
growth_rate	host-specific growth rate η_i	v(float)
death_rate	host-specific death rate μ_i	v(float)
carrying_capacity	K	v(integer)
infection_rate	host-specific infection coefficient γ_i	v(float)
segregation_error	host-specific rate of segregation error e_i	v(float(s))
perturbation_impact	host-specific degradation coefficient k_i	vfloat/0 w/o perturbation
plasmid_resistance	plasmid-specific plasmid resistance ρ_α	v(float)
plasmid_cost	plasmid-specific plasmid cost c_α	v(float)
A	host competition matrix A	v(v(float))
H	host HGT matrix H	v(v(integer))
I	plasmid infection matrix I	v(v(float(s)))
P	plasmid compatibility matrix P	v(v(float))
tensor_file	path to the JSON file of the propensity tensor	character

Table S7. Constants and parameters for the model performance test.

Variable	Definition	Value
t_{final}	time scale of the simulation	500
n	number of host and plasmid populations in the system	1:6
K	community-wise carrying capacity of host	1e4:2.1e5
e_i	probability of segregation error of host i	e-8
μ_i	per capita death rate of host i	0.015
η_i	per capita growth rate of host i	1.0
$\gamma_{i,p}$	infection coefficient of host subpopulation $H_{i,p}$	1e-4
ρ_α	resistance of plasmid α	1.0
c_α	cost of plasmid α on host growth	0.02
A	host competition matrix	$n \times n$ matrix of 1s
H	HGT matrix	$n \times n$ matrix of 1s
I	infection matrix	$n \times n$ matrix of 1s
P	plasmid compatibility matrix	$n \times n$ matrix of 1s and off-diagonal 0s

Table S8. Quantified modularity (Q) and nestedness (NODF) of the designed bipartite infection networks **I**. Q (between 0 and 1 for natural ecological networks) is computed following Barber (2007) [2], while NODF (between 1 and 100) is computed following Almeida-Neto et al. (2008) [3].

Network	Q	NODF
Full I	0.0	0
Nested I	≈ 0.1	100
Modular I	≈ 0.5	0

Table S9. Quantified Modularity (Qmax) and degree heterogeneity (H) of the designed unipartite plasmid compatibility networks **P**. Qmax (between 0 and 1 for natural ecological networks) is computed following Newman and Girvan (2004) [4], while H (between 0 and infinity; with 0.33 for a small network of four nodes indicating a star-like hub structure) is computed following Estrada (2010) [5].

Network	Qmax	H
Full P	0.0	0.0
Modular P	0.5	0.0
Hub P	0.0	≈ 0.33

References

1. Sprouffske K, Wagner A. Growthcurver: an R package for obtaining interpretable metrics from microbial growth curves. *BMC Bioinformatics*. 2016;17(1):172. doi:10.1186/s12859-016-1016-7.
2. Barber MJ. Modularity and community detection in bipartite networks. *Phys Rev E Stat Nonlin Soft Matter Phys*. 2007;76(6 Pt 2):066102. doi:10.1103/PhysRevE.76.066102.
3. Almeida-Neto M, Guimarães P, Guimarães PR Jr, Loyola RD, Ulrich W. A consistent metric for nestedness analysis in ecological systems: reconciling concept and measurement. *Oikos*. 2008;117(8):1227–1239. doi:10.1111/j.0030-1299.2008.16644.x.
4. Newman MEJ, Girvan M. Finding and evaluating community structure in networks. *Phys Rev E Stat Nonlin Soft Matter Phys*. 2004;69(2 Pt 2):026113. doi:10.1103/PhysRevE.69.026113.
5. Estrada E. Quantifying network heterogeneity. *Phys Rev E Stat Nonlin Soft Matter Phys*. 2010;82(6 Pt 2):066102. doi:10.1103/PhysRevE.82.066102.